Neurobiology of Disease 130 (2019) 104516

Contents lists available at ScienceDirect

Neurobiology of Disease

journal homepage: www.elsevier.com/locate/ynbdi

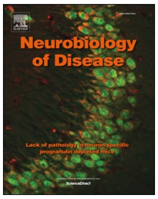

Ataxic phenotype with altered $Ca_V3.1$ channel property in a mouse model for spinocerebellar ataxia 42

Shunta Hashiguchi[a,1], Hiroshi Doi[a,1], Misako Kunii[a], Yukihiro Nakamura[b], Misa Shimuta[b], Etsuko Suzuki[b], Shigeru Koyano[a], Masaki Okubo[a], Hitaru Kishida[a], Masaaki Shiina[c], Kazuhiro Ogata[c], Fumiko Hirashima[d], Yukichi Inoue[e], Shun Kubota[a], Noriko Hayashi[a], Haruko Nakamura[a], Keita Takahashi[a], Atsuko Katsumoto[a], Mikiko Tada[a], Kenichi Tanaka[a], Toshikuni Sasaoka[f], Satoko Miyatake[g], Noriko Miyake[g], Hirotomo Saitsu[g], Nozomu Sato[h], Kokoro Ozaki[h], Kiyobumi Ohta[h], Takanori Yokota[h], Hidehiro Mizusawa[h], Jun Mitsui[i], Hiroyuki Ishiura[i], Jun Yoshimura[j], Shinichi Morishita[j], Shoji Tsuji[i], Hideyuki Takeuchi[a], Kinya Ishikawa[h], Naomichi Matsumoto[g], Taro Ishikawa[b,**], Fumiaki Tanaka[a,*]

[a] *Department of Neurology and Stroke Medicine, Yokohama City University Graduate School of Medicine, 3-9 Fukuura, Kanazawa-ku, Yokohama 236-0004, Japan*
[b] *Department of Pharmacology, The Jikei University School of Medicine, 3-25-8 Nishi-shinbashi, Minato-ku, Tokyo 105-8461, Japan*
[c] *Department of Biochemistry, Yokohama City University Graduate School of Medicine, 3-9 Fukuura, Kanazawa-ku, Yokohama 236-0004, Japan*
[d] *Department of Rehabilitation Medicine, Flower and Forest Tokyo Hospital, 2-3-6 Nishigahara, Kita-ku, Tokyo 114-0024, Japan*
[e] *Department of Neurology, Toyama Prefectural Rehabilitation Hospital and Support Center for Children with Disabilities, 36 Shimoiino, Toyama 931-8517, Japan*
[f] *Department of Comparative and Experimental Medicine, Center for Bioresource-based Researches, Brain Research Institute, Niigata University, 1-757 Asahimachidori, Chuo-ku, Niigata 951-8585, Japan*
[g] *Department of Human Genetics, Yokohama City University Graduate School of Medicine, 3-9 Fukuura, Kanazawa-ku, Yokohama 236-0004, Japan*
[h] *Department of Neurology and Neurological Science, Graduate School of Medical and Dental Sciences, Tokyo Medical and Dental University, 1-5-45 Yushima, Bunkyo-ku, Tokyo 113-0034, Japan*
[i] *Department of Neurology, Graduate School of Medicine, The University of Tokyo, 7-3-1 Hongo, Bunkyo-ku, Tokyo 113-8655, Japan*
[j] *Department of Computational Biology, Graduate School of Frontier Sciences, The University of Tokyo, 5-1-5 Kashiwanoha, Kashiwa, Chiba 277-8561, Japan*

ARTICLE INFO

Keywords:
Cerebellum
Spinocerebellar ataxia 42
CACNA1G
Knock-in mouse
Purkinje cell
Inferior olivary nucleus
Neurodegeneration
Electrophysiology

ABSTRACT

Spinocerebellar ataxia 42 (SCA42) is a neurodegenerative disorder recently shown to be caused by c.5144G > A (p.Arg1715His) mutation in *CACNA1G*, which encodes the T-type voltage-gated calcium channel $Ca_V3.1$. Here, we describe a large Japanese family with SCA42. Postmortem pathological examination revealed severe cerebellar degeneration with prominent Purkinje cell loss without ubiquitin accumulation in an SCA42 patient. To determine whether this mutation causes ataxic symptoms and neurodegeneration, we generated knock-in mice harboring c.5168G > A (p.Arg1723His) mutation in *Cacna1g*, corresponding to the mutation identified in the SCA42 family. Both heterozygous and homozygous mutants developed an ataxic phenotype from the age of 11–20 weeks and showed Purkinje cell loss at 50 weeks old. Degenerative change of Purkinje cells and atrophic thinning of the molecular layer were conspicuous in homozygous knock-in mice. Electrophysiological analysis of Purkinje cells using acute cerebellar slices from young mice showed that the point mutation altered the voltage dependence of $Ca_V3.1$ channel activation and reduced the rebound action potentials after hyperpolarization, although it did not significantly affect the basic properties of synaptic transmission onto Purkinje cells. Finally, we revealed that the resonance of membrane potential of neurons in the inferior olivary nucleus was decreased in knock-in mice, which indicates that p.Arg1723His $Ca_V3.1$ mutation affects climbing fiber signaling to Purkinje

---

Abbreviations: ACSF, Artificial cerebrospinal fluid; CF, Climbing fiber; DCN, Deep cerebellar nucleus; EPSC, Excitatory postsynaptic current; GFAP, Glial fibrillary acidic protein; ION, Inferior olivary nucleus; LTD, Long-term depression; PC, Purkinje cell; PF, Parallel fiber; pNF-H, Phosphorylated neurofilament heavy chain; SCA, Spinocerebellar ataxia; SR, Sag ratio; Ub, Ubiquitin

* Corresponding author at: Department of Neurology and Stroke Medicine, Yokohama City University Graduate School of Medicine, 3-9 Fukuura, Kanazawa-ku, Yokohama 236-0004, Japan.

** Correspondence to: T. Ishikawa, Department of Pharmacology, The Jikei University School of Medicine, 3-25-8 Nishi-shinbashi, Minato-ku, Tokyo 105-8461, Japan.

E-mail addresses: taroishi@jikei.ac.jp (T. Ishikawa), ftanaka@yokohama-cu.ac.jp (F. Tanaka).

[1] These authors contributed equally to this work.

https://doi.org/10.1016/j.nbd.2019.104516
Received 4 February 2019; Received in revised form 6 June 2019; Accepted 19 June 2019
Available online 20 June 2019
0969-9961/

cells. Altogether, our study shows not only that a point mutation in *CACNA1G* causes an ataxic phenotype and Purkinje cell degeneration in a mouse model, but also that the electrophysiological abnormalities at an early stage of SCA42 precede Purkinje cell loss.

1. Introduction

Spinocerebellar ataxia 42 (SCA42) is a newly discovered dominantly inherited type of SCA, the onset of which mainly occurs in young adulthood. It is reported as a predominantly pure form of slowly progressive ataxia, with atrophy of the cerebellum and severe degeneration of cerebellar Purkinje cells (PCs) (Coutelier et al., 2015). To date, ten families with SCA42, harboring a point mutation, c.5144G > A (p.Arg1715His), in calcium voltage-gated channel subunit alpha1 G (*CACNA1G*), have been reported: three families from a French study, four Japanese families, and one family each from the United States, Italy, and Yemen (Coutelier et al., 2015; Kimura et al., 2017; Morino et al., 2015; Ngo et al., 2018). However, pathological findings have been reported for only one case.

Voltage-gated calcium channels are classified into low-voltage-activated (T-type) and high-voltage-activated (L-, P/Q-, N-, and R-types) channels, based on their threshold for voltage-dependent activation (Cain and Snutch, 2011; Perez-Reyes and Lory, 2006; Simms and Zamponi, 2014). *CACNA1G* encodes one of the T-type voltage-gated calcium channels, $Ca_V3.1$, which is widely expressed in the brain, especially in neurons in the thalamus, hippocampus, and inferior olivary nucleus (ION), as well as cerebellar PCs (Ernst et al., 2009; Talley et al., 1999). $Ca_V3.1$ plays an important role in regulating calcium entry and membrane potential (Zamponi et al., 2015), including rebound burst firing of neurons in the thalamus (Kim et al., 2001) and cerebellar nuclei (Perez-Reyes and Lory, 2006; Tadayonnejad et al., 2010). Accordingly, $Ca_V3.1$ variants are associated with various disorders, including idiopathic generalized epilepsy (Singh et al., 2007), autism spectrum disorder (Strom et al., 2010), and more recently SCA42 and childhood-onset cerebellar atrophy (Chemin et al., 2018). Because of such diverse phenotypes caused by $Ca_V3.1$ variants, it is crucial to clarify the causal relationship between the p.Arg1715His mutation and the phenotype of SCA42.

Recent reports on SCA42 using overexpression systems in HEK293T cells found that the p.Arg1715His mutation caused a shift of $Ca_V3.1$ channel voltage dependence (Coutelier et al., 2015; Morino et al., 2015). However, whether this change occurs in neurons in endogenous tissues and whether the mutation is responsible for the SCA phenotype remain to be elucidated. In this paper, we first describe the clinical phenotype and pathological findings from a large Japanese family with SCA42, and then report findings in a newly generated knock-in (KI) mouse model of SCA42 harboring the p.Arg1723His mutation (*Cacna1g*-Arg1723His-KI mouse), which corresponds to the human p.Arg1715His mutation. In the model mice, we found an ataxic phenotype and PC degeneration, which recapitulated observations in human patients. Furthermore, electrophysiological analyses showed a shift of voltage dependence of $Ca_V3.1$ channels and altered action potential firing properties of PCs and neurons in ION. Thus, our study provides direct evidence that SCA42 is a channelopathy caused by a point mutation in *CACNA1G*.

2. Materials and methods

2.1. Patients

Ten affected and six unaffected members of a Japanese family with SCA were included in this study (Fig. 1A). Clinical information, radiological images, and blood samples were obtained from family members after written informed consent was provided. Experimental protocols were approved by the Institutional Review Boards of Yokohama City University (A180900002). All experiments were performed in accordance with institutional guidelines.

2.2. Structural analysis of the p.Arg1715His mutation in human $Ca_V3.1$

The structure of the region around Arg1715 in human $Ca_V3.1$ was modeled from the crystal structure of a homotetrameric sodium channel from *Arcobacter butzleri* (NavAb) (PDB code 3rvz) using the Phyre2 server (Kelley and Sternberg, 2009).

2.3. Animals

All animal experiments conformed to the Guide for the Care and Use of Laboratory Animals and were approved by the Institutional Committees of Laboratory Animal Experimentation (Animal Research Center of Yokohama City University, Yokohama, Japan; permission number: F-A-16-043; or the Institutional Animal Care and Use Committee of Jikei University; No. 2017-015).

Cacna1g Arg1723His-KI mice were generated using CRISPR/Cas9 technology. The single guide RNA (sgRNA) sequence was determined from the target sequence of mouse *Cacna1g* using the optimized CRISPR design tool (Hsu et al., 2013). A pair of oligonucleotides for the targeting site were ligated into the pX330 vector (Addgene, Cambridge, MA, USA) (Ran et al., 2013). Donor DNA was a manually designed, single-strand oligodeoxynucleotide (121 bp) with the following sequence:

5′-TTGAGGTCAATGCTTCACTGCCCATCAACCCCACCATCATCCGTATCATGAGGGTGCTCCACATTGCTCGAGGTAGGTCCAGCGCTTGTACCTGCCTTCCCCAGACGGAGATGGAAAGAGT-3′. A mixture of sgRNA-Cas9 expression vector (5 ng/μl) and donor oligonucleotide (100 ng/μl) was microinjected into the cytoplasm of fertilized eggs obtained from mating between C57BL/6NCrSlc males and superovulated females (Japan SLC, Hamamatsu, Japan). Injected eggs were then transferred into the uterus of pseudopregnant females. Genotyping of founder mice was performed by direct sequencing of PCR-amplified fragments from tail DNA using the BigDye Terminator V3.1 and 3500 Genetic Analyzer (Thermo Fisher Scientific, Waltham, MA, USA) with the following primers: 5′-TCAGAGAGCTGTGTTCCCGATTTTCCAGGT-3′ and 5′-GCTGGAGCTGGTGGGATGGTCCAC-3′. Selected founder mice were then crossed with C57BL/6NCrSlc mice and heterozygous KI mice were identified in the offspring. The entire genome editing procedure using CRISPR/Cas9 technology was performed by TransGenic Inc. (Fukuoka, Japan). Heterozygous mice were bred to obtain litter-matched homozygous, heterozygous, and wild-type (WT) control mice that were used in subsequent behavioral experiments. In electrophysiological experiments, homozygous mice obtained by homozygous breeding, heterozygous mice obtained by crossing homozygous and WT mice, and age-matched WT mice were used. Heterozygous, homozygous, and WT alleles were detected by PCR with the above primer set under the following cycling conditions: 2 min at 94 °C; then 10 s at 98 °C, 30 s at 63 °C, and 30 s at 68 °C for 35 cycles; followed by 5 min at 68 °C. For PCR reactions, KOD Plus Neo enzyme was used as a polymerase with standard PCR reagents (KOD401; Toyobo, Osaka, Japan). To distinguish each genotype, PCR products were digested with *Aci*I (R0551; New England BioLabs, Ipswich, MA, USA) and visualized by electrophoresis on 2% agarose gels. Sanger sequencing was performed to verify c.5168 G > A mutation in *Cacna1g*, with the mutation appropriately confirmed in homozygous, heterozygous, and WT strains. Animals were housed two to five per cage in square plastic cages with wire lids, under standard laboratory conditions (23 ± 2 °C) on a

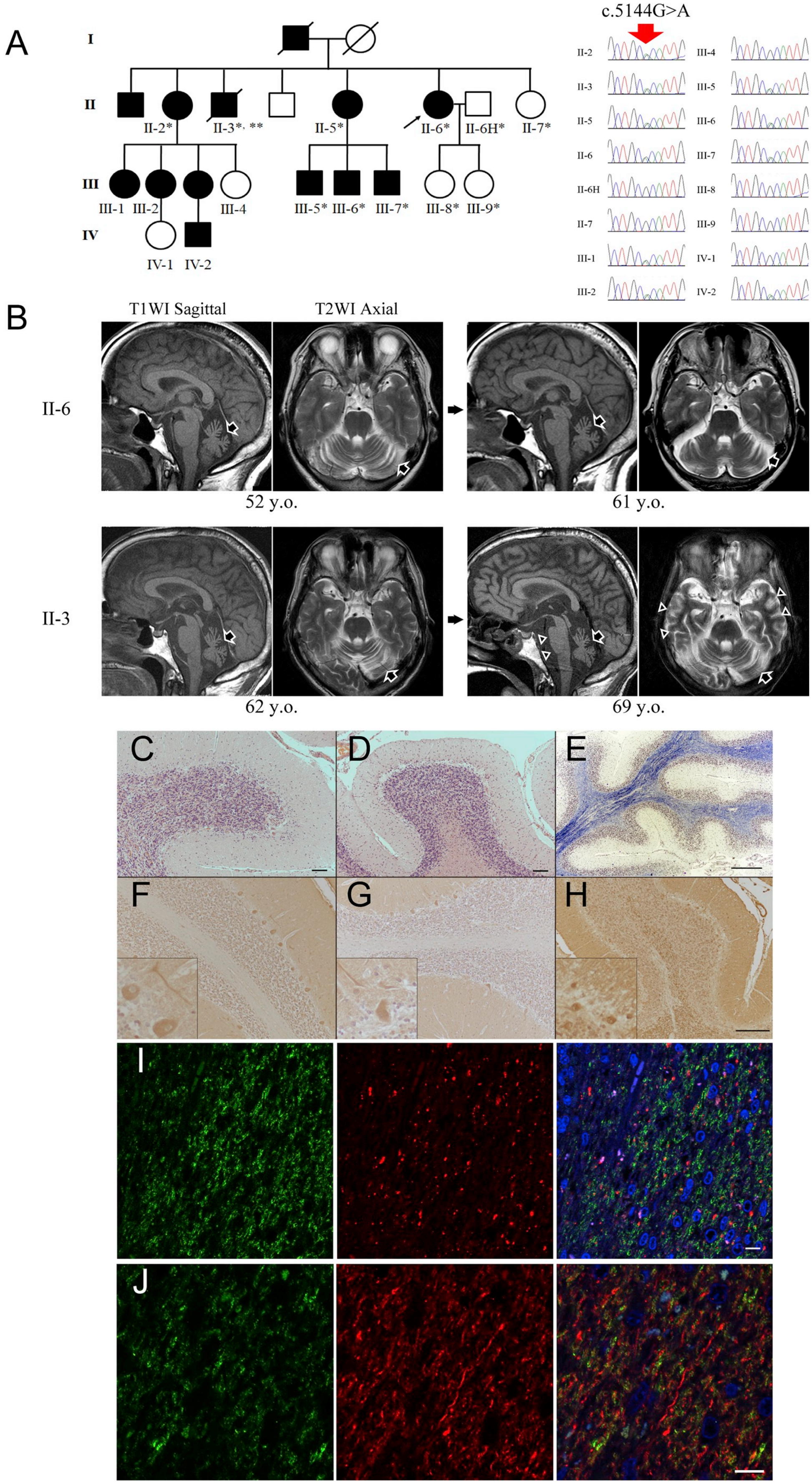

Fig. 1. SCA family with *CACNA1G* mutation.
(A) The left panel shows the family pedigree. Individuals with ID numbers are members whose genomic DNA was available, and an arrow indicates the proband. * indicates those whose genomic DNA was subjected to linkage analysis and exome sequencing. ** indicates the member used for pathological examination. With regard to the offspring of individual II-2, only those who participated in the study are described. The right panel shows electropherograms of the Sanger sequencing results. The single base substitution, c.5144G > A, is indicated by a red arrow. (B) Brain MRI of individuals II-6 (proband) and II-3 at the indicated age. Moderate cerebellar atrophy is observed in both cases (arrows), whereas cerebral atrophy (including hippocampal and brainstem atrophy) is only observed in II-3 (arrowheads). For each case, a T1-weighted image (T1WI) of a sagittal section and a T2-weighted image (T2WI) of an axial section are shown. Hematoxylin and eosin staining of the cerebellar hemisphere (C) and vermis (D). Bars indicate 100 μm. (E) Klüver–Barrera staining of the cerebellar white matter. Bar indicates 500 μm. Immunohistochemistry of the cerebellar cortex from the control (F), a cortical cerebellar atrophy patient (G), and the SCA42 patient (H) using anti-$\mathrm{Ca_V}3.1$ antibody. Magnified images are shown as insets. Bar indicates 200 μm. (I) Immunohistochemistry of the cerebellar white matter using anti-$\mathrm{Ca_V}3.1$ antibody (green) and anti-ubiquitin (Ub) antibody (red). The right panel shows an overlay of these two with DAPI staining (blue). Bar indicates 10 μm. (J) Immunohistochemistry of the cerebellar white matter using anti-$\mathrm{Ca_V}3.1$ antibody (green) and anti-pNF-H antibody (red). The right panel shows an overlay of these two with DAPI staining (blue). Bar indicates 10 μm. (For interpretation of the references to colour in this figure legend, the reader is referred to the web version of this article.)

light–dark cycle (light period, 05.00–19.00 h) and with free access to food and water. The body weight was measured once a week from the age of 4 to 50 weeks.

2.4. Behavioral experiments

Behavioral testing of heterozygous and homozygous *Cacna1g*Arg1723His-KI mice and their WT littermates (6–50 weeks old; all male) was performed during the light phase. A rotarod apparatus (model 47,650; Ugo Basile, Comerio, Italy) (Alfieri et al., 2014) was set at a constant speed of 5 rotations per minute (rpm) and mice were placed on it for 30 s on the first training day. On the following day, trials were repeated twice a day with at least 30-min intervals between them. The initial rotating speed was 5 rpm, which was gradually accelerated to 40 rpm over 300 s. Latency to fall was recorded. We placed the mice that fell off the rotarod during the first 30 s back onto the rotarod and did not use the data in those cases. Data are expressed as mean latency of the two trials (in seconds). In the hang wire test (Alfieri et al., 2014), mice were placed on top of a wire cage lid. The lid was then shaken gently to make each mouse hold tightly onto the wires, and then turned upside down and held 30 cm above the cage. We measured the latency until the mouse fell down into the cage. Mice that did not fall within the 60-s trial period were removed and assigned a time of 60 s. Mice were placed back on the lid if they fell down immediately or intentionally.

The gait of the mice was analyzed using a footprint test. Hindpaws and forepaws were immersed in blue and red watercolor, respectively, before they were allowed to walk on paper. Mice were prompted to walk straight across a white sheet (30 × 9 cm) surrounded by four cages. Before this test, mice were trained in two trials per day for 3 consecutive days. We measured the maximum width of the mass midpoints of bilateral hindpaw prints of at least five steps from the middle of each run (Ferdinandusse et al., 2008; Fujisawa et al., 2016).

2.5. Pathological evaluation

Brain specimens were obtained from postmortem examination of patient II-3 (Fig. 1A), a patient with cortical cerebellar atrophy (89 years old, female), and a control subject (78 years old, male) with cervical spondylotic myelopathy but without any neurodegenerative disorders. Informed consent was obtained from the family based on a protocol established by the Independent Review Boards of Yokohama City University School of Medicine. Autopsy of patient II-3 was performed 2 h after death, with the cause of death being rectal cancer. The investigation was limited to the brain and spinal cord. The brain was fixed in 10% formalin and cut into 1-cm-thick slices. Sliced tissue was embedded in paraffin wax, and 5-μm sections were subjected to conventional pathological analysis and immunohistochemical study. For immunohistochemical staining, sections were blocked in 0.1 M PBS containing 7% goat serum and 0.1% Triton X-100, and then incubated with primary antibody [mouse monoclonal anti-Ca$_V$3.1 antibody (MAB11559; Abnova, Taipei, Taiwan) (1:500), rabbit polyclonal anti-ubiquitin antibody (Z0458; DAKO Agilent Pathology Solutions, Santa Clara, CA, USA) (1:2000), and rabbit polyclonal anti-phosphorylated neurofilament heavy chain (pNF-H) antibody (R-1388-50; Biosensis, Thebarton, Australia) (1:1000)]. The reaction was enhanced with Vectastain ABC kit (RRID: AB_2336827; Vector Laboratories, Burlingame, CA, USA) and visualized with 3,3′-diaminobenzidine, as described by the manufacturer. Hematoxylin was used for counterstaining of sections in immunohistochemical study. For immunofluorescence staining, Alexa Fluor 488-conjugated anti-mouse-IgG (A-11017; Molecular Probes, Eugene, OR, USA) and Alexa Fluor 568-conjugated anti-rabbit-IgG antibody (A-11036; Molecular Probes) or Alexa Fluor 594-conjugated anti-rabbit-IgG antibody (A-11037; Molecular Probes) were used as secondary antibodies. Images were taken by an upright microscope equipped with a digital camera (ECLIPSE NiU; Nikon, Tokyo, Japan) or a confocal laser scanning microscope (FV1000; Olympus, Tokyo, Japan).

Mice were anesthetized with isoflurane and perfused transcardially with ice-cold phosphate-buffered saline (PBS; pH 7.4), followed by 4% paraformaldehyde. The brain was dissected out, post-fixed in 4% paraformaldehyde overnight at 4 °C, and then cut into 2-mm-thick slices. The slices were embedded in paraffin and sectioned at a thickness of 6 μm for conventional pathological analysis including hematoxylin/eosin (HE) and Klüver–Barrera (KB) staining. For immunohistochemical staining, primary antibodies [mouse monoclonal anti-Ca$_V$3.1 antibody (MAB11559; Abnova, Taipei, Taiwan) (1:500), rabbit polyclonal anti-Calbindin D-28 K antibody (RRID: AB_2068336; Millipore, Darmstadt, Germany) (1:500), and anti-glial fibrillary acidic protein (GFAP) antibody (RRID: AB_2571556; Frontier Science Co., Ltd., Ishikari, Japan) (1:200)] were used at the indicated dilutions. Secondary antibodies, and the methods of immunohistochemistry and image capture were the same as described above. The total number of PCs, the length of the PC layer, and the areas of the molecular layer and total cerebellum in the HE-stained sagittal section of the vermis were measured using “free hand selections” in ImageJ software (Schneider et al., 2012).

2.6. Electrophysiology and analysis

Mice were deeply anesthetized with isoflurane and decapitated. The brain was rapidly removed and immersed in ice-cold oxygenated slicing solution containing the following (in mM): 235 sucrose, 2.5 KCl, 1.25 Na_2HPO_4, 6 $MgCl_2$, 2 Na pyruvate, 3 myo-inositol, 0.5 Na ascorbate, 26 $NaHCO_3$, and 10 D-glucose, with bubbling with 95% O_2 and 5% CO_2. Parasagittal slices (300 μm thick) of the cerebellar vermis or transverse slices (300 μm thick) of the brainstem containing ION were cut using a vibratome (Linear Slicer Pro7, Dosaka EM, Kyoto, Japan). Slices were incubated at 34 °C for 30 min and thereafter maintained at room temperature. The composition of artificial cerebrospinal fluid (ACSF) for incubation and recording was (in mM): 125 NaCl, 2.5 KCl, 1.25 Na_2HPO_4, 1 $MgCl_2$, 2 $CaCl_2$, 2 Na pyruvate, 3 myo-inositol, 0.5 Na ascorbate, 26 $NaHCO_3$, and 10 D-glucose, with bubbling with 95% O_2 and 5% CO_2. Whole-cell voltage-clamp recordings were obtained from PCs using either Axopatch 200B or Multiclamp 700B amplifiers (Molecular Devices, San Jose, CA, USA). For calcium current recording, ACSF was supplemented with 3 μM tetrodotoxin (TTX) citrate, 1 mM tetraethylammonium (TEA)-Cl, 5 mM 4-aminopyridine, 1 mM CsCl, 5 μM 2,3-dihydroxy-6-nitro-7-sulfamoyl-benzo[*f*]quinoxaline-2,3-dione (NBQX), and 10 μM bicuculline methiodide to block voltage-gated Na^+ and K^+ currents and synaptic currents. Patch pipettes with 2–6 MΩ resistance were filled with internal solution containing the following (in mM): 120 CsCl, 20 TEA-Cl, 10 HEPES, 10 EGTA, 4 ATP-Mg, 0.5 Na_2GTP (pH 7.3, 299 mOsm). To isolate Ca$_V$3.1 current, ω-agatoxin IVA (400 nM; Peptide Institute, Ibaraki, Japan) and ω-conotoxin GVIA (2 μM; Peptide Institute) were applied together with cytochrome C (0.1 mg/ml). Series resistance was typically 4–18 MΩ, which was compensated by 75%–85%. Liquid junction potential (2.5 mV) was not corrected. Leak and capacitive currents were subtracted using a P/6 protocol. Current–voltage curves (IV curves) were obtained from normalized T-type calcium currents resulting from 200-ms voltage steps. Activation curves were calculated from normalized relative conductance–voltage plots and fitted with a Boltzmann equation: $G/G_{max} = 1/(1 + \exp.(V_{1/2} - V_m)/k)$, where G was calculated as $G = I/(V_m - E_{rev})$. Here, $V_{1/2}$ represents the half-activation potential; V_m, membrane potential; E_{rev}, reversal potential; k, slope factor; G, conductance; G_{max}, maximum conductance; I, current at a given V_m; and I_{max}, maximum current. E_{rev} was estimated by linear fitting of peak amplitudes from −15 to +15 mV. For steady-state inactivation curves, normalized relative conductance–voltage plots were calculated from the voltage step to −20 mV after incremental depolarizing pulses (duration = 500 ms). Inactivation curves were fitted to $I/I_{max} = 1/(1 + \exp.(V_m - V_{1/2})/k)$. Here, $V_{1/2}$ represents the half-inactivation potential.

Current-clamp recordings were obtained from PCs and from ION neurons. The pipette solution contained (in mM): 132 K-methanesulfonate, 7 KCl, 10 HEPES, 0.1 EGTA, 2 ATP-Mg, 2 Na_2ATP, 0.5 Na_2GTP (pH adjusted to 7.2 with KOH). Liquid junction potential (8 mV) was not corrected. Cells with resting membrane potential higher than −45 mV and cells that required hyperpolarizing currents > 600 pA to maintain the holding potential below −70 mV were discarded. To assess hyperpolarization-activated current (I_h), we used the sag ratio (SR): $SR = (V_{rest} - V_{rebound}) / (V_{rest} - V_{min})$, where V_{min} is the minimal potential achieved at the beginning of the current step, V_{rest} is the resting membrane potential, and $V_{rebound}$ is the steady-state potential estimated by the mean over the last 100 ms of the pulse (van Welie et al., 2006). Resonance of ION neurons was measured by injecting a sinusoidal current with a constant amplitude (400 pA) with frequency gradually changing from 1 to 18 Hz in 20 s in the presence of 1 μM TTX. The magnitude of the complex impedance was calculated by dividing the fast Fourier transform of the voltage response by that of the command current. Resonance strength was defined as the maximum impedance magnitude normalized by the impedance magnitude at 1 Hz (Matsumoto-Makidono et al., 2016).

Excitatory postsynaptic currents (EPSCs) were recorded from PCs. Patch solution contained (in mM): 110 Cs methanesulfonate, 30 CsCl, 10 HEPES, 0.5 EGTA, 4 ATP-Mg, 0.5 Na_2GTP (pH 7.3, 310 mOsm). To block inhibitory synaptic currents, 100 μM picrotoxin was added to ACSF. For climbing fiber (CF) stimulation, the tip of the stimulating glass electrode was placed in the granular layer, typically ~100 μm away from the soma of a recorded PC. To reduce the amplitude of recorded currents and improve voltage-clamp conditions, PCs were clamped at −20 mV (Matsushita et al., 2002). For parallel fiber (PF) stimulation, the tip of the stimulating glass electrode was placed in the molecular layer. PCs were voltage-clamped at −70 mV. EPSCs were evoked every 10–15 s. Series resistance was typically 5–10 MΩ after compensation and kept constant throughout each experiment by gentle pressure or adjustment of compensation. Paired-pulse ratio was defined as the ratio of the second EPSC amplitude relative to the first. For recording spontaneous inhibitory postsynaptic current (sIPSC) from PCs, we used the same internal solution as in calcium current recording and ACSF containing 5 μM NBQX to block EPSCs. Since the chloride reversal potential was near 0 mV in this condition, sIPSC was recorded as inward current at the holding potential of −70 mV. sIPSC events were recorded for at least 60 s and detected off-line using an amplitude threshold algorithm (TaroTools), a custom-written macro in Igor Pro (WaveMetrics, Portland, OR, USA). Long-term depression (LTD) was induced by pairing PF stimuli in conjunction with PC depolarization. This conditioning stimulus consisted of 10 blocks applied every 10 s. Each block involved five consecutive PF stimulations (50 Hz) followed by 10 ms of depolarization of PCs to 0 mV with a latency of 40 ms. During conditioning stimulus series resistance, compensation was omitted to ensure depolarization of dendritic arbors. The magnitude of LTD was defined by the change in EPSC amplitude at 25–30 min after the conditioning stimulus compared with a 5-min baseline immediately preceding the conditioning. All electrophysiological recordings were performed at room temperature. We used immature (P6–9) mice for the recording of voltage-gated calcium currents from PCs because the extended dendritic arbor in older mice hampers voltage-clamp control of the cell (Llano et al., 1994). We used P12–18 mice for current-clamp recording from PCs, and P19–24 mice for all other recordings, considering the most suitable balance between the degree of postnatal maturation and cell viability in brain slices. TTA-P2 and TTX were from Alomone Labs, Ltd. (Jerusalem, Israel). All other chemicals for electrophysiology were from Nacalai Tesque (Kyoto, Japan) or Wako Chemicals (Osaka, Japan).

Data were low-pass-filtered at 2–5 kHz and digitized at 10–20 kHz using Clampex 10 (Molecular Devices). Data were analyzed using Clampfit 10.7 or NeuroMatic (Rothman and Silver, 2018) in Igor Pro. The coefficient of variation (CV) of interspike intervals (ISI) was calculated as CV = (standard deviation of ISI) / (mean of ISI). Due to the long tail of ISI distribution, the longest 5% of ISIs were removed from calculation of CV. Another index, CV2, which reflects local variability of ISI, was calculated as $CV2 = \text{mean of } 2 \times |ISI_{n+1} - ISI_n| / (ISI_{n+1} - ISI_n)$.

2.7. *Statistical analysis*

Statistical analyses were performed using Prism 7 (GraphPad Software, La Jolla, CA, USA) or Igor Pro. To compare two groups, unpaired *t*-test was used when the data were assumed to follow a normal distribution. To compare three groups, one-way ANOVA with post hoc Tukey's test was used when the sample distribution of the data was assumed to be normal, while Kruskal–Wallis test with post hoc Dunn's test was used in other cases. All data are presented as mean ± SEM, with $P < 0.05$ considered significant.

3. Results

3.1. *Clinical features*

Among the family members, 13 individuals were affected by ataxic symptoms; detailed clinical information and DNA were available for 10 of them (Fig. 1A and Table S1). The age of onset of motor symptoms was concentrated in young adulthood, ranging from 13 to 32 years old. The principal feature of the affected members was a cerebellar syndrome with or without slight pyramidal signs. Among the affected members, one had a learning disability and progressive dementia (II-3), another had severe psychiatric problems such as aggressive behavior and delusions (III-6), and three had truncal myoclonus (II-2, III-5, and III-7). Brain MRI revealed moderate cerebellar atrophy. Cerebral or brainstem atrophy was not observed in individual II-6 (Fig. 1B). In individual II-3, who had learning disability and progressive dementia (and underwent postmortem evaluation), progressive cerebral and brainstem atrophy was observed, in addition to cerebellar atrophy (Fig. 1B).

As a result of linkage analysis, two candidate regions covering approximately 27.8 Mb, and with a maximum LOD score of 2.4, were identified (Table S2). In these regions, whole-exome sequencing of the family members identified c.5144G > A (p.Arg1715His) of *CACNA1G* (NM_018896.4) as the disease cause.

3.2. *Pathological examinations*

We also performed a postmortem pathological examination of patient II-3. Neuropathological examination of this patient identified significant changes in the cerebellar cortex and white matter, and mild atrophy of cerebrum and brainstem. Specifically, the cerebellar cortex showed severe loss of Purkinje and granule cells. In addition, the molecular layer was thinner than normal (Fig. 1C–E). These changes were more pronounced in the vermis than in the hemisphere (Fig. 1C, D). The cerebellar white matter showed myelin pallor, fibrillary gliosis, and spongiform changes (Fig. 1E). However, α-synuclein- or tau-positive aggregates were not detected in the cerebellum, pons, or medulla oblongata, while only a small number of neurofibrillary tangles were observed in the hippocampus and parahippocampal gyrus (Table 1). Immunohistochemistry for $Ca_V3.1$ was performed using the reactivity-confirmed antibody (Supp. Fig. S1). $Ca_V3.1$ immunoreactivity was observed in the cytoplasm of Purkinje cells, dentate nucleus neurons, ION neurons, and dendritic and axonal processes in cerebellar and cerebral cortex (Table 1). We did not detect $Ca_V3.1$-immunoreactive inclusions in the cytoplasm or nucleus of neurons and glia in the cerebellar cortex (Fig. 1H, I). Interestingly, $Ca_V3.1$ immunoreactivity was increased in cerebellar white matter in the SCA42 patient compared with that in a control without any neurodegenerative diseases and that in a patient with cortical cerebellar atrophy (Fig. 1F–H). However, such anti-$\mathrm{Ca_V}$3.1 reactivity did not colocalize with either Ub-positive deposits or immunoreactivity for an axonal marker, phosphorylated neurofilament heavy chain (pNF-H) (Fig. 1I, J). The other pathological findings are summarized in Table 1.

3.3. Analysis of mutation effect by 3D modeling of Arg1715 residue and intracellular distributions of the channels

We examined the effect of the p.Arg1715His mutation on $\mathrm{Ca_V}$3.1 by mapping it onto a modeled 3D structure. Human $\mathrm{Ca_V}$3.1 is composed of four homologous domains (domains I–IV) [each of which consists of six transmembrane helices (termed S1–S6)] and shares a similar topology with sodium ion channels. In $\mathrm{Ca_V}$3.1, the amino acid sequence of the S4 segment of domain IV is well conserved with the corresponding region in the bacterial voltage-gated sodium channel (NavAb). Thus, we mapped the mutation site of human $\mathrm{Ca_V}$3.1 onto the crystal structure of bacterial NavAb (PDB code 3rvz) (Fig. 2A, B). Arg1715 in $\mathrm{Ca_V}$3.1 corresponds to Arg102 in NavAb, and is a charged residue that plays a significant role in voltage-sensing and gating (Payandeh et al., 2011). In the crystal structure of NavAb, the side chain of Arg102 forms a hydrogen bond with the main chain of the loop region between the S3 and S4 segments to maintain their local conformation. This indicates that the p.Arg1715His mutation would result in loss of the hydrogen bond and the gating charge, leading to impairment of the gating function.

To further investigate the effect of the mutation, we examined the intracellular distribution of WT and p.Arg1715His mutant $\mathrm{Ca_V}$3.1. Upon subcellular fractionation of HEK293T cells expressing the channels followed by western blotting, WT and mutant $\mathrm{Ca_V}$3.1 showed similar subcellular distributions (Supp. Fig. S1B). Immunocytochemistry revealed that overexpressed WT and mutant $\mathrm{Ca_V}$3.1 were similarly located in the plasma membrane (Supp. Fig. S1C).

3.4. Establishment of Cacna1g-Arg1723His-KI mice presenting with ataxic phenotype

Using the CRISPR/Cas9 system, we generated KI mice harboring the p.Arg1723His mutation in *Cacna1g*, which corresponds to human p.Arg1715His mutation (Coutelier et al., 2015) (Fig. 3A). Sanger sequencing confirmed single base substitution of c.5168G > A in *Cacna1g* (Fig. 3B). Heterozygous and homozygous *Cacna1g*-Arg1723His-KI mice (hereafter, simply KI mice) and their WT littermates showed no difference in body weight, which increased over time (Fig. 3C). To assess motor coordination and balance, we used the accelerated rotarod test. Although all mouse genotypes showed similar performance until 10 weeks old, at older ages both heterozygous and homozygous KI mice fell off the rotarod with significantly reduced latencies compared with WT mice (Fig. 3D). No significant difference was seen between heterozygous and homozygous KI mice (see Fig. 3 legend for P-values). This poor performance was stably maintained up to 50 weeks old. However, in the wire hang test, both KI mice showed latency to fall similar to that of WT mice (Fig. 3E), suggesting that grip strength remained intact. Footprint patterns at 50 weeks old showed that the maximum width of the mass midpoints of bilateral hindpaw prints was greater in KI mice than in WT (Fig. 3F). These behavioral tests demonstrate that heterozygous and homozygous KI mice develop motor impairments due to ataxia rather than muscle weakness. These findings are consistent with the human SCA42 phenotype.

3.5. Progressive cerebellar degeneration in Cacna1g-Arg1723His-KI mice

To investigate pathological changes, we compared sagittal sections of cerebellar vermis from each genotype, where the loss of PCs was apparent in the human postmortem specimen (Fig. 1C). HE and KB stains showed that the cerebellar cortex of KI mice was indistinguishable from that of the WT up to 15 weeks old. However, in heterozygous and homozygous KI mice at 50 weeks old, degeneration of PCs became discernible (Fig. 4A). PC density in 50-week-old heterozygous and homozygous KI mice was reduced compared with that in each phenotype at 15 weeks old, and that in WT mice at 50 weeks old (Fig. 4B). In addition, the area proportion of the molecular layer relative to the whole cerebellum in 50-week-old homozygous KI mice was decreased compared with that at 15 weeks, whereas that in WT and heterozygous KI mice remained unchanged (Fig. 4C). GFAP staining also revealed increased reactive astrocytes in homozygous KI mice at 50 weeks old, supporting the occurrence of neurodegeneration (Fig. 4A). In contrast, anti-Cav3.1 antibody immunoreactivity in the PC cytoplasm did not differ among the genotypes. There were no visible ubiquitin-positive deposits in WT, heterozygous, or homozygous KI mice (Supp. Fig. S2). The morphology of the soma and dendrites of PCs stained with anti-

Table 1
Summary of pathological findings of the II-3 patient.

	Degeneration (HE staining)	Ub reactivity	1C2 reactivity	Tau reactivity	α-Synuclein reactivity	TDP-43 reactivity	$\mathrm{Ca_V}$3.1 reactivity
Cerebral cortex	–	–	–	±			
Hippocampus	–	–		+			
Cerebral white matter	+ (spongiform)	+					
Caudate nucleus	–						
Putamen	–						
Pallidum	–						
Thalamus	–						
Oculomotor nucleus	±	+ (Marinesco body)	–		–		
Red nucleus	±	–	–		–		
Substantia nigra	+	–	–		±		
Pontine nucleus	±	–	–				±
Locus ceruleus	±	–	–				
Hypoglossal nucleus	–						
Inferior olivary nucleus	–						±
Anterior horn	–					–	
Cerebellum	+ + Vermis > hemisphere	Small deposits in white matter					White matter
Cerebellar cortex (Purkinje cells)	+ +	–					+
Cerebellar cortex (granular layer)	+ +	–					±
Cerebellar cortex (molecular layer)	+ +	–					+
Dentate nucleus	±	–					+

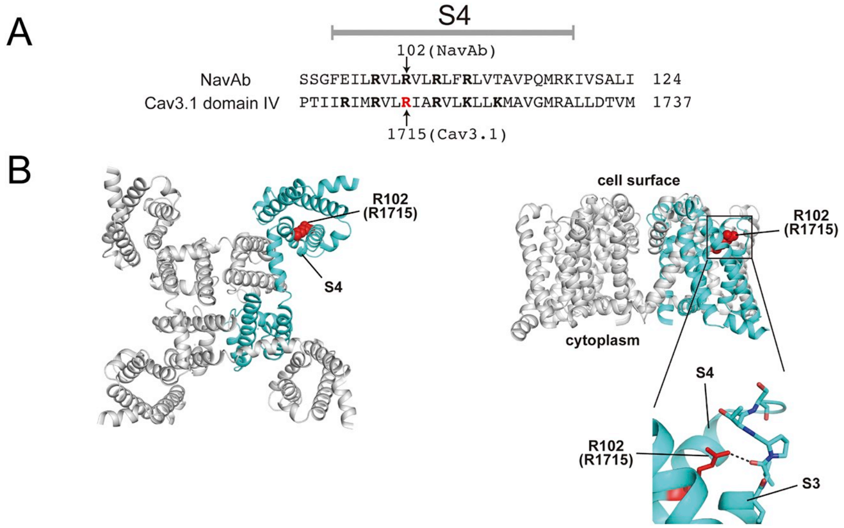

Fig. 2. 3D modeling of Arg1715 residue.
(A) Pairwise alignment of amino acid sequences from the S4 transmembrane segment in domain IV of the human low-voltage calcium channel ($Ca_V3.1$) and in the bacterial voltage-gated sodium channel (NavAb). The conserved basic residues are shown in bold face. (B) The crystal structure of NavAb (PDB code 3rvz) (Payandeh et al., 2011) viewed from the intracellular side of the membrane (left) and parallel to the membrane plane (right), with a magnified view of the boxed region. In the magnified view, residues within the loop region between the S3 and S4 segments are shown in the stick representation with oxygen and nitrogen atoms in red and blue, respectively. One subunit of a homotetramer is colored cyan, and the others in gray. Arg102 in NavAb (corresponding to Arg1715 in $Ca_V3.1$) is shown as red van der Waals spheres in the overview and red sticks in the magnified view. A black dashed line depicts a hydrogen bond. (For interpretation of the references to colour in this figure legend, the reader is referred to the web version of this article.)

calbindin antibody did not show a clear difference among the genotypes, although the loss of PCs in homozygous mice was apparent at 50 weeks old (Fig. 4D). Apart from the cerebellar cortex, there was no obvious difference in cell density or any morphological change of neurons of both deep cerebellar nucleus (DCN) and ION among the genotypes at 50 weeks old (Fig. 4E). Moreover, we did not find pathological changes in other areas in the brainstem and the cerebrum where the human case (II-3) showed mild atrophic changes. These results indicated that p.Arg1723His mutation triggers neurodegeneration of cerebellar cortex, especially in PCs.

3.6. *Altered voltage dependence of T-type calcium currents in cerebellar PCs of Cacna1g-Arg1723His mice*

Cacna1g is highly expressed in cerebellar neurons, especially PCs (Engbers et al., 2013). To investigate the impact of $Ca_V3.1$ mutation on channel function in situ, we performed whole-cell voltage-clamp recording of T-type calcium currents from PCs in acute cerebellar slices. In the presence of P/Q- and N-type calcium channel blockers, the remaining currents elicited by depolarizing voltage steps in PCs are thought to be T-type calcium currents (Fig. 5A). Indeed, T-type calcium channel blocker TTA-P2 (3 μM) blocked the remaining currents to a large extent. The maximum amplitudes of T-type calcium current were similar among the genotypes. However, when we plotted normalized current amplitude against command voltage, we found a rightward shift of the curves in mutant $Ca_V3.1$ (Fig. 5B). Half-activation potential in homozygous KI mice was significantly more positive than in WT mice, although that in heterozygous KI mice was not significantly different from that in WT mice (Fig. 5C). Slope factors were similar among the genotypes [WT: 3.83 ± 0.38 mV, Hetero: 3.20 ± 0.53 mV, Homo: 3.80 ± 0.36 mV] (Fig. 5C). There was no significant effect of the mutation on half-inactivation potential [WT ($n = 7$): −60.8 ± 2.05 mV, Hetero ($n = 7$): −59.8 ± 1.31 mV, Homo ($n = 8$): −61.9 ± 0.88 mV] or slope factor [WT: 9.40 ± 0.94 mV, Hetero: 10.2 ± 0.70 mV, Homo: 9.90 ± 0.41 mV] (Fig. 5C). In addition, no significant differences were observed in activation, inactivation, and deactivation speed ($n = 6$ cells for each genotype) (Fig. 5D–F). These results demonstrate that p.Arg1723His mutation changes the voltage dependence of T-type calcium currents in native PCs.

3.7. *Reduced rebound firing in PCs with Arg1723His $Ca_V3.1$ channels*

To determine whether the change in voltage dependence of $Ca_V3.1$ mutation could affect firing properties, we performed current-clamp recording from PCs of presymptomatic juvenile mice (P12–23). In WT PCs, we observed spontaneous firing (27.2 ± 2.63 Hz; $n = 11$ cells from 6 mice) at the resting membrane potential (−53.5 ± 0.66 mV) (Fig. 6A). Heterozygous and homozygous mutant PCs showed similar resting potentials (Fig. 6B), spontaneous firing frequencies [Hetero ($n = 11$ cells from 5 mice): −51.8 ± 1.02 mV, 29.9 ± 3.58 Hz, Homo ($n = 9$ cells from 6 mice): −54.1 ± 1.38 mV, 31.4 ± 5.40 Hz] (Fig. 6C), and threshold of spontaneous firing (WT: −45.2 ± 1.4 mV, Hetero: −42.8 ± 2.1 mV, Homo: −46.1 ± 1.5 mV, $P = 0.408$; one-way ANOVA). The regularity of spontaneous firing evaluated using CV of ISI and CV2 index (see Materials and Methods) was also similar among the genotypes (CV: WT, 0.19 ± 0.027, Hetero, 0.13 ± 0.014, Homo, 0.13 ± 0.026, $P = 0.291$, CV2: WT, 0.16 ± 0.028, Hetero, 0.09 ± 0.014, Homo, 0.13 ± 0.034, $P = 0.213$; one-way ANOVA). Mean firing rates during current injection (from −1 nA to 3 nA) did not differ among WT, heterozygous, and homozygous KI mice (Fig. 6D). However, rebound excitation following hyperpolarizing current injection triggered significantly fewer spikes in both heterozygous and homozygous KI PCs than in WT PCs (Fig. 6E). TTA-P2 diminished the number of rebound firings in all genotypes, indicating that T-type calcium channel activity was crucial for the rebound firing. In addition, sag ratios, which reflect I_h current (see Materials and Methods), did not differ significantly among the genotypes (Fig. 6F). These results suggest that $Ca_V3.1$ p.Arg1723His mutation can dampen PC excitability immediately after hyperpolarization.

3.8. *Synaptic properties of PCs in Cacna1g-Arg1723His-KI mice*

We next determined whether synaptic function is impaired in PCs of KI mice before the onset of PC degeneration. In all cells examined, climbing fiber-mediated EPSCs (CF-EPSCs) (Fig. 7A) occurred in an all-or-none manner when the stimulus intensity was gradually changed. The amplitude of CF-EPSCs was similar between genotypes (Fig. 7B). When a pair of stimuli were administered with inter-stimulus intervals of 10–500 ms, paired-pulse depression was observed in both WT and KI mice in a similar manner (Fig. 7C). The amplitude of parallel fiber-mediated EPSCs (PF-EPSCs) gradually increased with increasing stimulus intensity. When the stimulus intensity was set to evoke EPSCs of ~500 pA in amplitude (Fig. 7D), we did not detect significant differences in the rise time (10%–90%: WT, 1.55 ± 0.08 ms, Hetero, 1.51 ± 0.22 ms, Homo, 1.43 ± 0.15 ms) or decay time constant (WT, 7.0 ± 0.6 ms, Hetero, 7.0 ± 0.7 ms, Homo, 6.5 ± 0.8 ms) of PF-EPSCs. When a pair of stimuli were administered, paired-pulse facilitation was observed in both WT and homozygous KI mice in a similar manner (Fig. 7E). To study whether the mutation in $Ca_V3.1$ affects the inhibitory synaptic inputs onto PCs, we recorded spontaneous

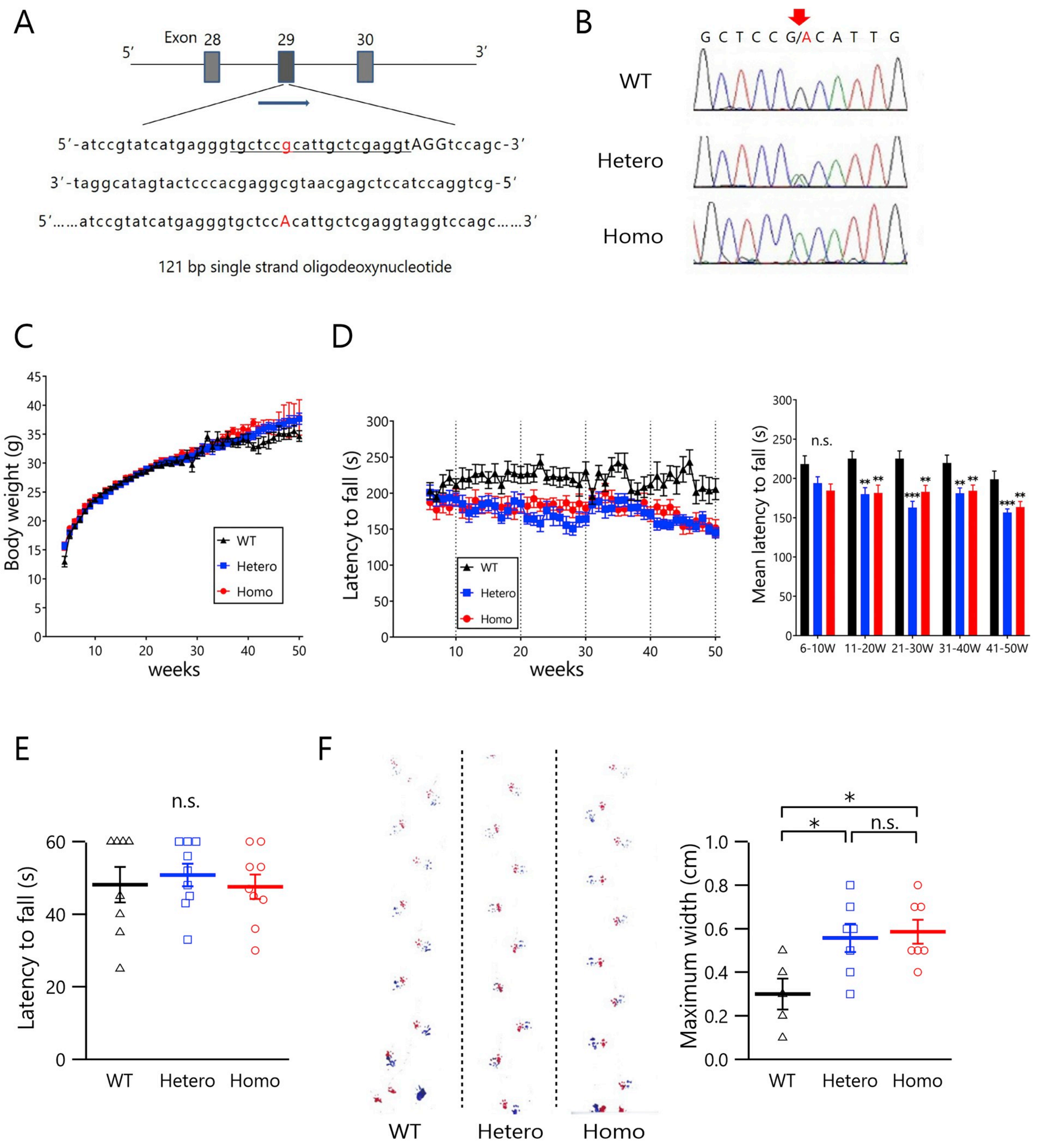

Fig. 3. Generation and phenotypic analysis of *Cacna1g*-Arg1723His-KI mice.

(A) Scheme of the target site at the *Cacna1g* (mouse chromosome 11, NC_000077.6) locus. Protospacer adjacent motif (PAM) sequence is shown in upper-case letters, with the single guide RNA target underlined. In the donor DNA, the single-strand oligodeoxynucleotide and replaced nucleotide are indicated by upper-case, red letters. (B) Electropherograms of Sanger sequencing for the target site of wild-type (WT) mice (top), heterozygous (middle), and homozygous knock-in (KI) offspring (bottom). Single base substitution of c.5168G > A in *Cacna1g* is indicated by an arrow. (C) Body weight curves of WT littermates (black), and heterozygous (blue) and homozygous KI mice (red) at ages from 4 to 50 weeks. No significant differences were detected between WT and either genotype of KI mice. (D) Accelerated rotarod performance (5–40 rpm/5 min) from 6 to 50 weeks (left panel). The average latency to fall during every section showed that both heterozygous and homozygous KI mice demonstrated worsening of motor performance compared with WT mice (right panel) [6–10 weeks: WT (n = 14) vs. Hetero (n = 15), P = 0.39, WT vs. Homo (n = 15), P = 0.09, Hetero vs. Homo, P = 0.67; 11–20 weeks: WT vs. Hetero, P = 0.003, WT vs. Homo, P = 0.004, Hetero vs. Homo, P = 0.99; 21–30 weeks: WT vs. Hetero, P < 0.0001, WT vs. Homo, P = 0.0039, Hetero vs. Homo, P = 0.23; 31–40 weeks: WT vs. Hetero, P = 0.0043, WT vs. Homo, P = 0.0092, Hetero vs. Homo, P = 0.96; 41–50 weeks: WT vs. Hetero, P = 0.0009, WT vs. Homo, P = 0.0056, Hetero vs. Homo, P = 0.78, Tukey's multiple comparison test]. (E) Wire hang test. No significant differences in grip strength were detected between WT mice and either genotype of KI mice from 36 to 40 weeks old. A cut-off time of 60 s was adopted. WT (n = 8), Hetero (n = 9), Homo (n = 9), P = 0.85; Kruskal–Wallis test. (F) Footprint test. Representative footprints from mice with each genotype (red, forepaws; blue, hindpaws). The maximum width of the mass midpoints of bilateral hindpaw prints of KI mice was significantly greater than that of WT mice. WT (n = 5), vs. Hetero (n = 7), P = 0.035, WT vs. Homo (n = 7), P = 0.019; Tukey's multiple comparison test. ***P < 0.001; **P < 0.01; *P < 0.05. Error bars indicate SEM. (For interpretation of the references to colour in this figure legend, the reader is referred to the web version of this article.)

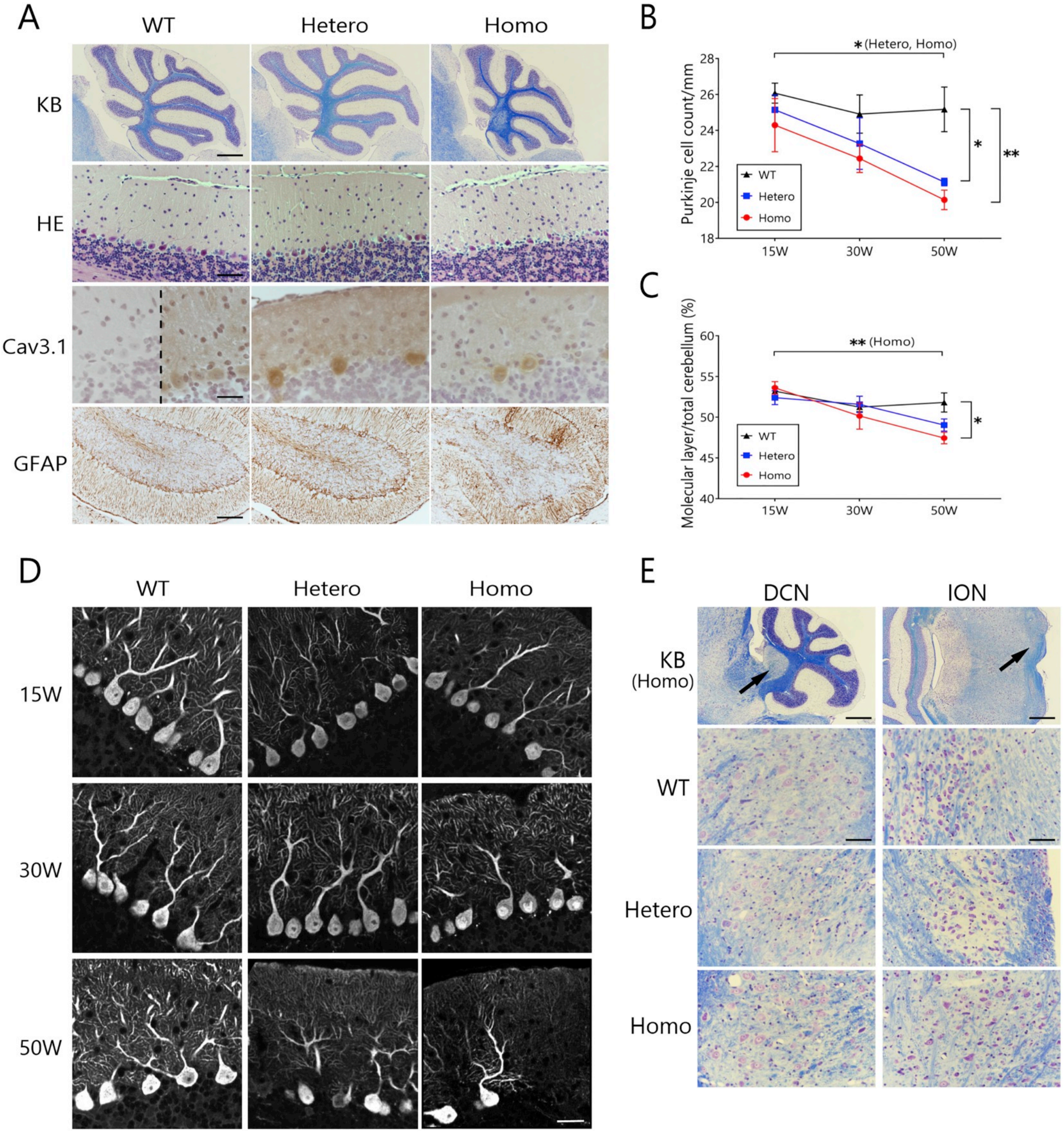

Fig. 4. Pathological evaluation of the cerebellum of *Cacna1g*-Arg1723His-KI mice.
(A) KB (top row) and HE (second row) staining of the cerebellar vermis from wild-type (WT) mice (50 weeks old), heterozygous mice (50 weeks old), and homozygous mice (50 weeks old), and immunohistochemical staining of the cerebellar vermis from each genotype using anti-Cav3.1 [third row (right panel), including negative control with no primary antibody (left panel)] and anti-GFAP (bottom row) antibodies. Bars indicate 500, 50, 25, and 100 μm (from top to bottom). (B) Quantitative analysis of Purkinje cell (PC) density in the vermis of cerebellum at 15, 30, and 50 weeks old. Hetero: 25.1 ± 0.83 cells/mm (15 weeks old, n = 4) vs. 21.1 ± 0.21 cells/mm (50 weeks old, n = 4), P = 0.039, Homo: 24.3 ± 1.48 cells/mm (15 weeks old, n = 6) vs. 20.1 ± 0.54 cells/mm (50 weeks old, n = 5), P = 0.049, WT: 25.2 ± 1.24 cells/mm (50 weeks old, n = 4), WT vs. Hetero at 50 weeks old, P = 0.012, WT vs. Homo at 50 weeks old, P = 0.002; Tukey's multiple comparison test. (C) Changes in the ratio of the molecular layer to the total cerebellum at 15, 30, and 50 weeks old. Hetero: 15 vs. 50 weeks old, n = 4, P = 0.054, Homo: 15 vs. 50 weeks old, n = 5, P = 0.0026. WT (n = 4) vs. Hetero (n = 4) at 50 weeks old, P = 0.13, WT vs. Homo (n = 5) at 50 weeks old, P = 0.013; Tukey's multiple comparison test. (D) Immunofluorescent staining of the cerebellar vermis from WT, heterozygous, and homozygous mice using anti-calbindin antibody over time. Bar indicates 20 μm. (E) Representative images with KB staining at low magnification of both DCN and ION obtained from homozygous genotypes (indicated by arrows) (top row, bars indicate 500 μm). The following images at high magnification were obtained from each genotype (50 weeks old). Bars indicate 50 μm. Statistical significance was assessed by one-way ANOVA with Tukey's multiple comparison test. **P < 0.01; *P < 0.05. Error bars indicate SEM.

inhibitory postsynaptic currents (sIPSCs, Fig. 7F) from basket or stellate cells (Orduz and Llano, 2007; Wulff et al., 2009). We found that both frequency and amplitude of sIPSCs were similar among genotypes (Fig. 7G), suggesting that inhibitory synaptic function was not impaired in KI mice.

Rising calcium in PC dendrites is essential for the induction of LTD in PF-EPSCs (Sakurai, 1990). Although the primary channel for calcium entry into dendrites is $Ca_V2.1$, activation of dendritic $Ca_V3.1$ may additionally contribute to rising calcium during the formation of LTD (Isope and Murphy, 2005). To examine whether the mutation in $Ca_V3.1$ might affect the LTD, we compared the extent of LTD formation between wild-type and homozygous KI mice. We adopted a relatively mild conditioning stimulus (see Materials and Methods) to avoid LTD saturation. Using this protocol, we were able to induce LTD in WT mice (Fig. 7H) (EPSC reduction, 48 ± 10% measured after 25–30 min, n = 5 cells from 2 mice). In homozygous KI mice, LTD was induced to a similar extent [40 ± 7%, n = 7 cells from 5 mice] (Fig. 7H). All of these experiments suggest that the basic property of synaptic transmission onto PCs is not significantly impaired in young KI mice.

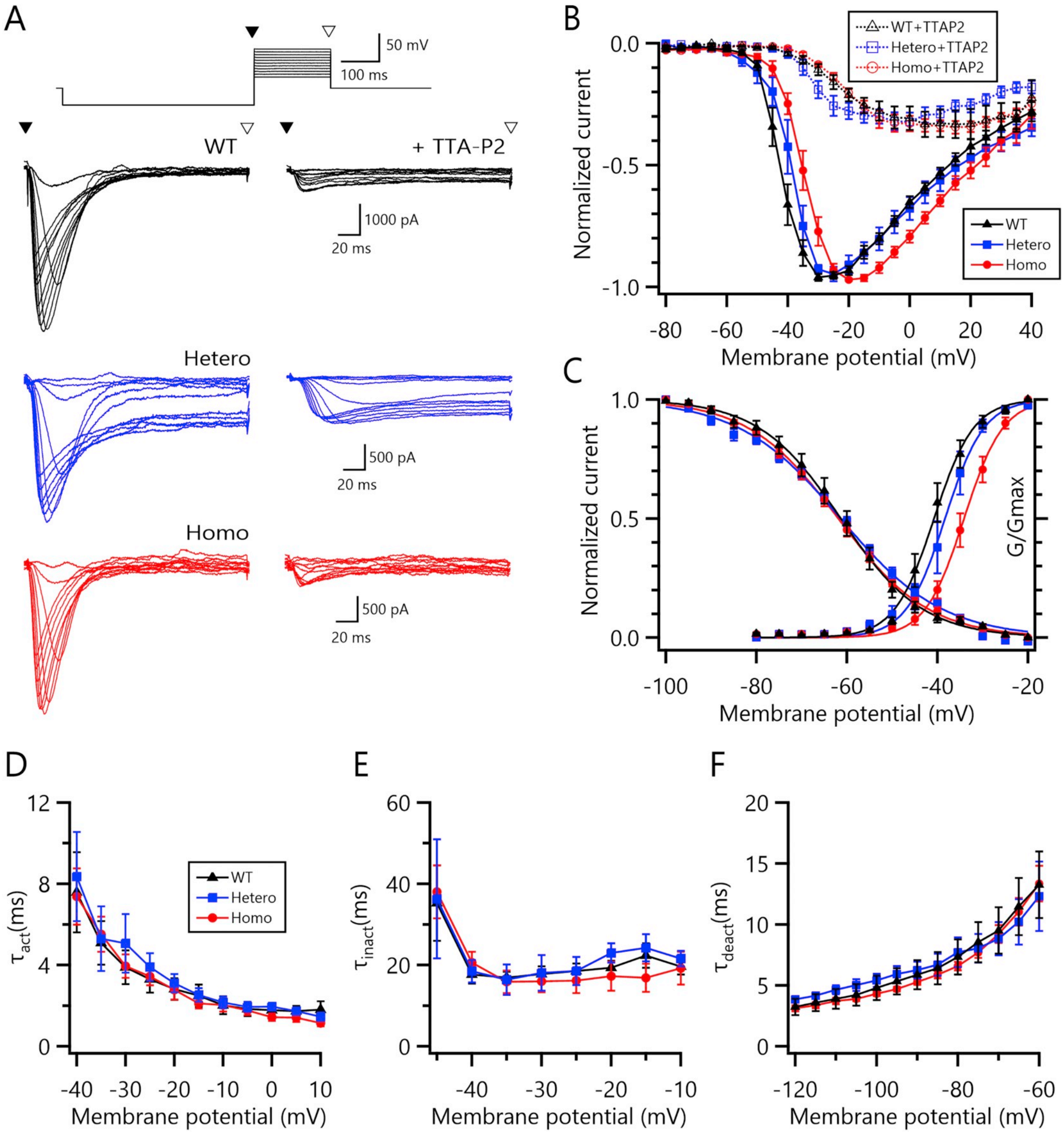

Fig. 5. Voltage-clamp analysis of T-type calcium currents of WT and Arg1723His mutant $Ca_V3.1$ channels.
(A) T-type calcium currents were recorded from Purkinje cells (PCs). Top panel represents command voltage steps (5 mV increments) for 200 ms, preceded by a hyperpolarizing step to −100 mV. Black, blue, and red traces are representative calcium current recordings from WT mouse, heterozygous, and homozygous knock-in (KI) mice, respectively, before (left) and after (right) 3 μM TTA-P2 treatment. Representative traces between −50 and 0 mV are shown (5 mV increments). The maximum amplitudes of T-type calcium current were similar among the genotypes [WT: 1972 ± 510 pA, Hetero: 1134 ± 275 pA, Homo: 1499 ± 202 pA, P = 0.282; one-way ANOVA]. (B) Current–voltage (IV) curves. Normalized IV plots of T-type calcium currents from PCs of WT (black), and heterozygous (blue) and homozygous KI mice (red) with (outlined symbols) or without (solid symbols) TTA-P2 treatment show a positive shift of the activation voltage in mutant $Ca_V3.1$. (C) Steady-state activation and inactivation voltage curves. Half-activation potentials were − 40.2 ± 1.10 mV in WT mice (n = 9 cells from 7 mice, black), − 38.3 ± 1.46 mV in heterozygous KI mice (n = 8 cells from 8 mice, blue), and − 34.1 ± 1.08 mV in homozygous KI mice (n = 9 cells from 8 mice, red) (WT vs. Hetero, P = 0.53, WT vs. Homo, P = 0.0035, Homo vs. Hetero, P = 0.054; Tukey's multiple comparison test), while slope factors were similar (WT: 3.83 ± 0.38 mV, Hetero: 3.20 ± 0.53 mV, Homo: 3.80 ± 0.36 mV, P = 0.517; one-way ANOVA). There was no significant effect of the mutation on half-inactivation potential [WT (n = 7): −60.8 ± 2.05 mV, Hetero (n = 7): −59.8 ± 1.31 mV, Homo (n = 8): −61.9 ± 0.88 mV, P = 0.60; one-way ANOVA] and slope factor [WT: 9.40 ± 0.94 mV, Hetero: 10.2 ± 0.70 mV, Homo: 9.90 ± 0.41 mV, P = 0.73; one-way ANOVA]. (D, E) Time constant of activation (D) and inactivation (E) kinetics. Curves were obtained by fitting calcium current traces after depolarizing stimulations (shown in A) with single exponential functions. (F) Time constant of deactivation kinetics [WT (n = 6), Hetero (n = 6), Homo (n = 6)]. Deactivating calcium currents during various voltage steps after a fixed voltage step from −100 to −30 mV (duration = 20 ms) were fitted with single exponential functions. Error bars indicate SEM. (For interpretation of the references to colour in this figure legend, the reader is referred to the web version of this article.)

3.9. Resonance in ION neurons of Cacna1g-Arg1723His- KI mice

We next set out to assess whether there is underlying change in the properties of neurons in ION. It has been suggested that Cav3.1 in ION plays an important role in amplifying a property called "resonance" of membrane potential (Matsumoto-Makidono et al., 2016). Resonance is a property that enhances the oscillation of membrane potential (thus increasing the impedance) at a preferred frequency (Hutcheon and Yarom, 2000; Puil et al., 1986). To assess this property, we applied sinusoidal current injection using a "ZAP" command current in the presence of TTX (see Materials and Methods). In WT mice, the impedance became highest at 5.9 ± 0.7 Hz (n = 9 cells from 4 mice) in a manner depending on the setting of the resting membrane potential (Fig. 8A). In heterozygous (Fig. 8B) and homozygous KI mice (Fig. 8C), the frequency at which the impedance magnitude peaked (max. frequency) was 6.2 ± 0.6 Hz (n = 9 cells from 3 mice) and 7.8 ± 0.8 Hz

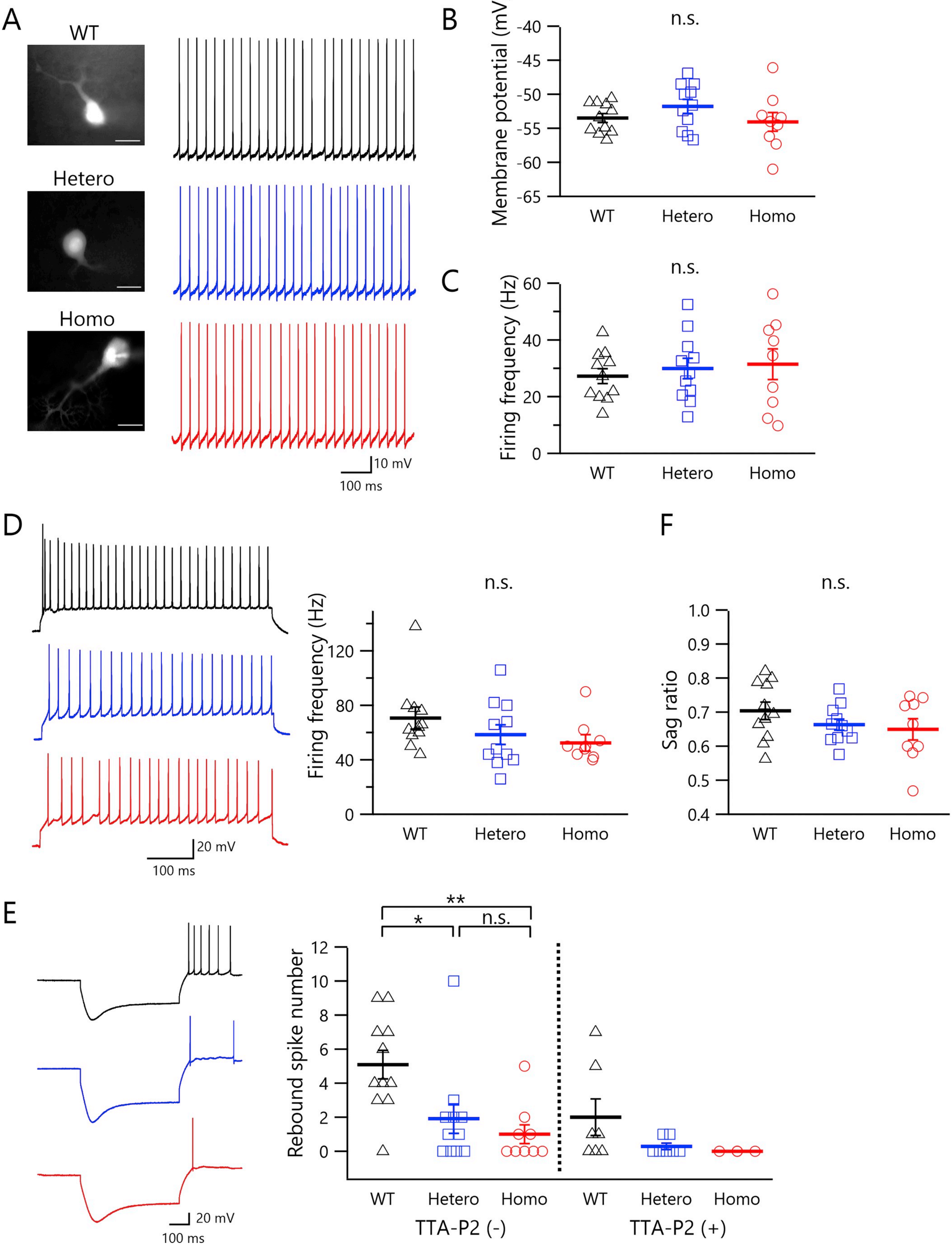

(caption on next page)

Fig. 6. Action potential firings in PCs of WT and Arg1723His $Ca_V3.1$ channels.
(A) Spontaneous firing activity in PCs from wild-type (WT) (upper), and heterozygous (Hetero) (middle) and homozygous (Homo) (lower) KI mice. Left panels show fluorescence images of representative PCs (scale bar, 25 μm). (B, C) Resting membrane potential (B) and spontaneous firing frequency (C) of PCs [WT (n = 11 cells from 6 mice): −53.5 ± 0.66 mV, 27.2 ± 2.63 Hz, Hetero (n = 11 cells from 5 mice): −51.8 ± 1.02 mV, 29.9 ± 3.58 Hz, Homo (n = 9 cells from 6 mice): −54.1 ± 1.38 mV, 31.4 ± 5.40 Hz, P = 0.28, P = 0.74, respectively; one-way ANOVA]. (D) *Left*, Representative PC firing activity in WT (black), heterozygous (blue), and homozygous (red) mice in response to depolarizing current injection at 0.5 nA from −70 mV. *Right*, The mean firing frequency calculated from the number of spikes during 500-ms step 0.5 nA currents [WT: 70.5 ± 7.54 Hz, Hetero: 58.4 ± 7.24 Hz, Homo: 53.3 ± 5.08 Hz, P = 0.21; one-way ANOVA]. (E) Rebound spikes in each genotype. *Right*, Number of rebound spikes of PCs before (left) and after (right) TTA-P2 treatment [WT vs. Hetero, P = 0.031, WT vs. Homo, P = 0.0046, Hetero vs. Homo, P > 0.999; Kruskal–Wallis test with Dunn's multiple comparison test]. (F) Sag ratio distribution in each genotype when current of −1.0 nA was injected. There was no significant difference among the genotypes [WT: 0.70 ± 0.025, Hetero: 0.66 ± 0.016, Homo: 0.65 ± 0.031, P = 0.28; one-way ANOVA. **P < 0.01; *P < 0.05]. Error bars indicate SEM. (For interpretation of the references to colour in this figure legend, the reader is referred to the web version of this article.)

(n = 8 cells from 3 mice), respectively, similar to that in the WT (Fig. 8D). To evaluate the impedance magnitude, we defined the impedance strength, which was significantly lower in homozygous KI mice (2.7 ± 0.4) than in WT mice (6.0 ± 0.9). The impedance strength of heterozygous mice (3.8 ± 0.7) fell between those of WT and homozygous mice, but the difference between heterozygous mice and WT was not statistically significant (Fig. 8E). These results suggest that Arg1723His $Ca_V3.1$ mutation might disturb the firing of ION neurons, thereby affecting CF signaling to PCs.

4. Discussion

Here, we have described a Japanese family with SCA, specifically, the largest family with SCA42 reported to date (Fig. 1 and Table S1). Consistent with the clinical presentation described in previous reports (Coutelier et al., 2015; Kimura et al., 2017; Morino et al., 2015; Ngo et al., 2018; Sato et al., 2010), the main phenotype in our patients was slowly progressive ataxia with onset mainly in young adulthood. Among the family members, one patient had a learning disability, while another had severe psychiatric issues. Truncal myoclonus, which was not a previously described symptom, was occasionally observed in three of the ten patients. In previous reports, 3 of 42 informative patients with *CACNA1G* mutations were described as having depression (Coutelier et al., 2015; Kimura et al., 2017; Morino et al., 2015; Ngo et al., 2018; Sato et al., 2010). In addition to a very slowly progressive cerebellar syndrome, the presence of truncal myoclonus and cognitive and/or psychiatric symptoms in some family members might be indicative of SCA42. Currently, the mechanisms for this intra- and inter-familial phenotypic variability are unclear. It is also unknown whether p.Arg1715His mutation might directly cause truncal myoclonus. Although it has been reported that other mutations in *CACNA1G* (p.Ala570Val and p.Ala1089Ser) may cause idiopathic generalized epilepsy, including juvenile myoclonic epilepsy (JME), those mutations did not lead to clear dysfunction of the channels (Singh et al., 2007). Thus, truncal myoclonus in SCA42 may be caused by a mechanism distinct from that in JME.

The present study is the first to report immunohistochemical analysis of a patient's specimen. The patient (II-3) who underwent postmortem examination not only showed motor symptoms but also had learning disability and progressive dementia. In this individual, no pathological evidence of Alzheimer's disease, dementia with Lewy bodies, or other tauopathies was observed, indicating that the cerebral atrophy might be a direct or indirect consequence of *CACNA1G* mutation. Immunostaining with anti-ubiquitin antibody revealed ubiquitin-positive nuclear inclusions in the oculomotor nucleus, but they were compatible with nonspecific Marinesco bodies (Beach et al., 2004). Thus, no specific ubiquitin-positive aggregates had formed in the patient. On a related issue, although we noted that $Ca_V3.1$ immunoreactivity was high in the cerebellar white matter, it is unlikely that this reactivity reflected any specific protein aggregation, because (1) mutant $Ca_V3.1$ did not show abnormal localization in cultured cells (Supp. Fig. S1C), (2) $Ca_V3.1$-positive inclusions were absent from neurons in the surveyed regions, (3) the $Ca_V3.1$ reactivity did not colocalize with ubiquitin (Fig. 1H), and (4) the $Ca_V3.1$ reactivity also did not colocalize with the axonal marker pNF-H (Fig. 1I). Therefore, it is likely that the accumulation of $Ca_V3.1$ was a secondary change due to white matter degeneration rather than specific protein accumulation, which might be observed in other dominantly inherited conformational diseases such as CAG repeat diseases.

We assessed the motor coordination of SCA42 model mice using the rotarod and footprint tests (Fig. 3D, F). Remarkably, both heterozygous and homozygous KI mice demonstrated an adult-onset mild ataxic phenotype, recapturing the essential clinical feature of SCA42. Although homozygous KI mice were slightly more prone to severe PC loss and degeneration of the molecular layer (Fig. 4), heterozygous and homozygous mice showed comparable levels of motor impairment (Fig. 3D), corresponding to dominant inheritance of SCA42. These results indicate that the mutation causes an ataxic phenotype by a process distinct from a simple loss-of-function mechanism because previous reports show that *Cacna1g* knockout mice have normal growth, normal brain morphology (Kim et al., 2001), and no motor impairment (Park et al., 2010), albeit with some abnormalities including non-REM sleep disturbance (Lee et al., 2004). Furthermore, transgenic mice overexpressing wild-type $Ca_V3.1$ do not show an ataxic phenotype either (Ernst et al., 2009). Against this background, the present study is the first to report that *Cacna1g*-modified mice have a phenotype related to SCA. While our mice recapitulated slowly progressive ataxia, the principal phenotype of SCA42, it is yet to be examined whether other phenotypes found in some family members, like truncal myoclonus and the cognitive and/or psychiatric symptoms, may also exist in the model mice. Studies using further behavioral tasks are needed to address this issue.

The relationship between PC dysfunction and the motor phenotype in other degenerative ataxia models has been investigated (Hansen et al., 2013; Jayabal et al., 2015; Shakkottai et al., 2011). Our pathological evaluation of SCA42 model mice revealed degeneration of PCs, as seen in human SCA42 (Table 1 and Fig. 1), in 50-week-old heterozygous and homozygous KI mice and atrophic thinning of the molecular layer in 50-week-old homozygous KI mice (Fig. 4B, C). Using anti-$Ca_V3.1$ antibody, we confirmed that mutant $Ca_V3.1$ channels do not form neuronal inclusions or abnormal distributions (Fig. 4A). Considering that the ataxic phenotype was already apparent at 11–20 weeks of age (when PC degeneration had not occurred), triggering of the ataxic phenotype in KI mice might be attributable to functional changes, rather than simple loss of PCs (Fig. 3D and Fig. 4B).

A shift of voltage-dependent activation of $Ca_V3.1$ induced by p.Arg1715His mutation has been reported in HEK293T-cell overexpression systems (Coutelier et al., 2015; Morino et al., 2015). In the present study, we showed that the mutation indeed altered the voltage dependence of activation of T-type calcium currents toward positive in native PCs in the same manner (Fig. 5). Arg1715 is located in the S4 segment, which undergoes outward displacement, and initiates central pore opening in response to depolarization (Payandeh et al., 2011). Our structural consideration revealed that Arg1715 consists of a gating charged residue, which forms a hydrogen bond with the main chain of the loop region between the S3 and S4 segments (Fig. 2B). Such a

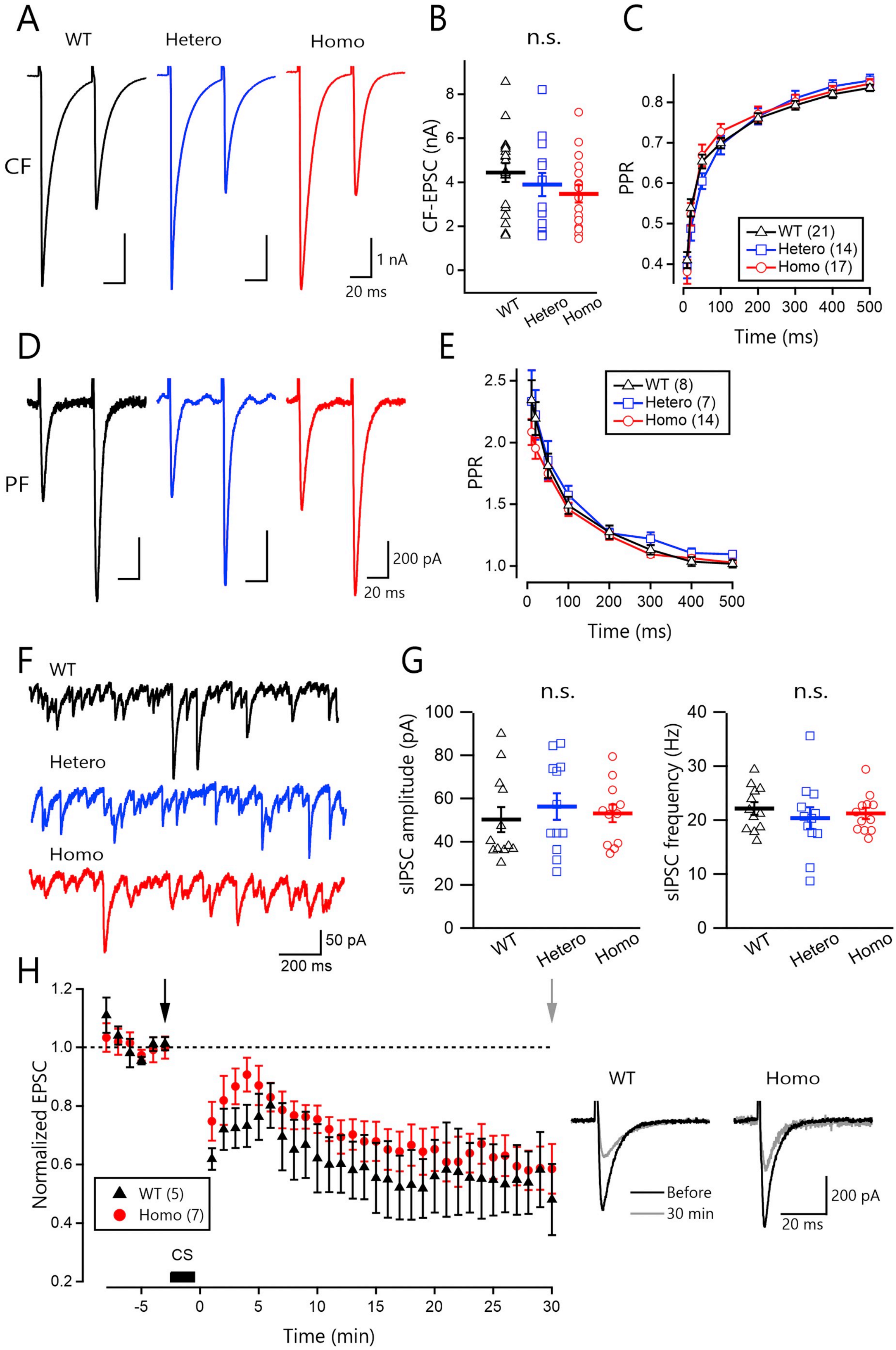

(caption on next page)

Fig. 7. Excitatory and inhibitory synaptic transmission onto PCs.
(A) Representative traces of CF-mediated EPSCs from WT (left), and heterozygous (center) and homozygous mutant (right) PCs. To evaluate paired-pulse ratio (the ratio of the second EPSC amplitude relative to the first), the stimulus was applied twice with an interval of 50 ms. (B) The amplitude of CF-mediated EPSCs recorded at a holding potential of −20 mV. WT: 4.3 ± 0.7 nA, n = 11 cells from 5 mice, Hetero: 4.5 ± 0.7 nA, n = 9 cells from 3 mice, Homo: 3.4 ± 0.5 nA, n = 12 cells from 4 mice, P = 0.43; one-way ANOVA. (C) Paired-pulse ratio of CF-mediated EPSCs at various inter-stimulus intervals. (D) Representative traces of PF-mediated EPSCs from WT (left), and heterozygous (center) and homozygous mutant (right) PCs. (E) Paired-pulse ratio of PF-mediated EPSCs. (F) Representative traces of spontaneous IPSC from WT mice (upper), heterozygous mice (middle), and homozygous mice (bottom). (G) Both mean frequency and amplitude of spontaneous IPSC are similar in PCs (frequency: WT: 22.1 ± 1.18 Hz, n = 12 cells from 3 mice, Hetero: 20.4 ± 1.98 Hz, n = 12 cells from 3 mice, Homo: 21.2 ± 1.02 Hz, n = 12 cells from 3 mice, P = 0.68; amplitude: WT: 50.2 ± 5.74 nA, Hetero: 56.2 ± 6.10 nA, Homo: 53.0 ± 4.05 nA, P = 0.73; one-way ANOVA). (H) Time course of long-term depression (LTD). EPSC amplitudes were normalized by a mean of 5 min before the conditioning stimulus (CS). Arrows represent the time point for correcting representative traces shown in the right panel. *Right*, representative traces of PF-EPSCs from WT (left) and homozygous mutant (right) PCs immediately before (black) and 30 min after (gray) induction of the conditioning stimulus. Traces show a mean of six consecutive events (WT: 48 ± 10%, n = 5 cells from 2 mice, Homo: 40 ± 7%, n = 7 cells from 5 mice, P = 0.48; unpaired *t*-test). Error bars indicate SEM.

structural role of Arg1715 may underlie the changes in voltage-sensitivity of calcium channels described above. These findings on calcium channel properties were in clear contrast to those in recent reports showing no detectable change in calcium current in a cellular model of SCA6, which is caused by trinucleotide CAG repeat expansion in *CACNA1A*, the gene coding P/Q-type calcium channel (Bavassano et al., 2017; Watase et al., 2008). Our study demonstrates a distinct pathophysiological basis of SCA42 compared with that in SCA6 and that the missense mutation of $Ca_V3.1$ with the physiological expression level could directly cause alterations of channel property, progressive ataxia, and PC degeneration.

We found a significant decrease of rebound firing of PCs after hyperpolarization in KI mice (Fig. 6E). These results suggest that even a modest change in voltage dependence of T-type calcium channels has a significant impact on the rebound firing of PCs. T-type calcium channels are thought to transform neuronal output to a burst mode by generating

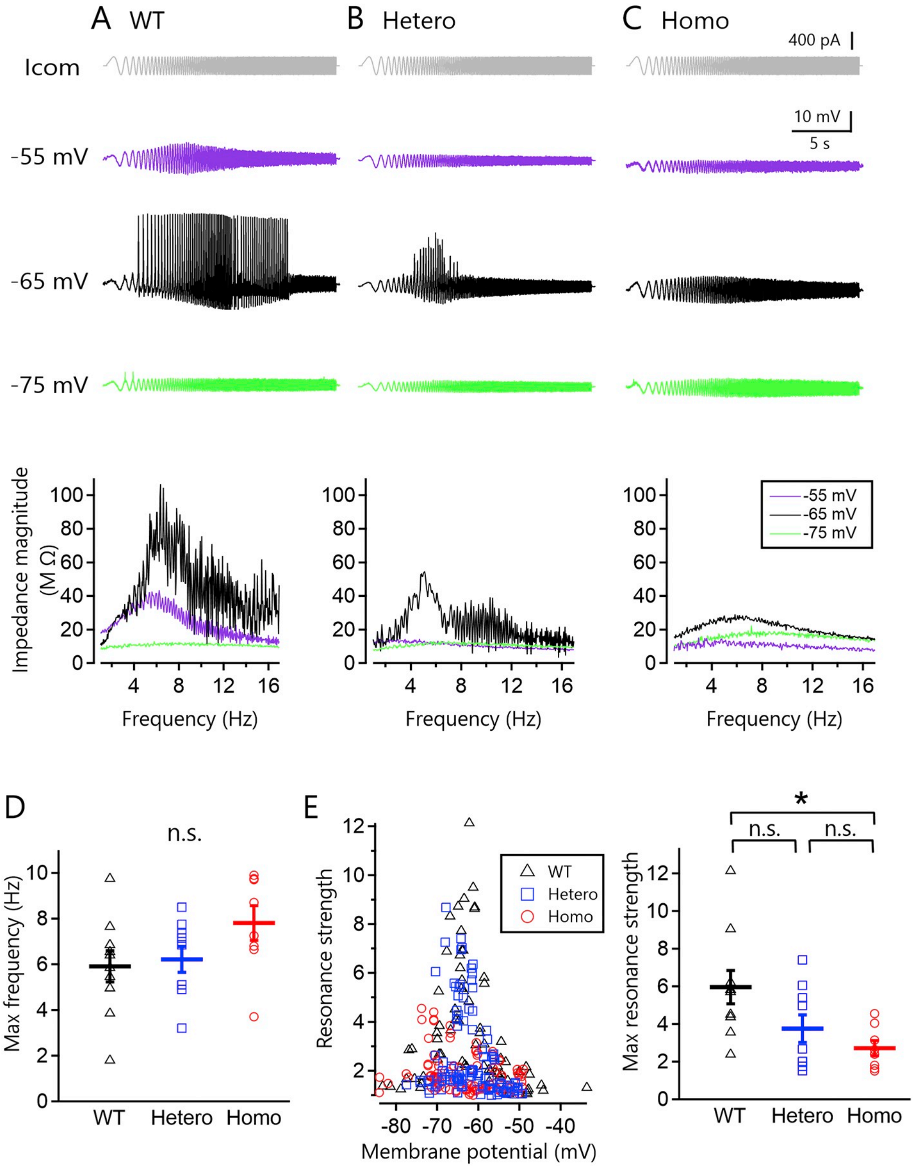

Fig. 8. Resonance in ION neurons.
(A) Representative voltage waves in response to ZAP stimulus current (top gray, 400 pA in amplitude) at −55 mV (light blue), −65 mV (black), and − 75 mV (blue) in wild type. Bottom panel represents the impedance–frequency profile calculated from the above traces. (B) The same as A but ION neurons from hetero mutant mouse. (C) The same as A but ION neurons from homo mutant mouse. (D) Maximum frequency, defined as the frequency at which impedance peaked, is plotted for each genotype. (E) *Left*, Resonance strength, defined as the ratio of maximum impedance amplitude to impedance amplitude at 1 Hz, is plotted against membrane potential. All recordings at various membrane potentials from multiple cells are superimposed. *Right*, Summary plot of maximum resonance strength. Each data point represents the maximum resonance strength for a given cell. WT (n = 10 cells from 4 mice), vs. Hetero (n = 9 cells from 3 mice), P = 0.10, WT vs. Homo (n = 8 cells from 3 mice), P = 0.014, Hetero vs. Homo, P = 0.61; Tukey's multiple comparison test. *P < 0.05. Error bars indicate SEM. (For interpretation of the references to colour in this figure legend, the reader is referred to the web version of this article.)

low-voltage-activated calcium currents and rebound burst discharge in the thalamus and DCN (Molineux et al., 2006; Perez-Reyes and Lory, 2006). They might also play similar roles in cerebellar PCs (De Schutter and Bower, 1994). As a general rule, the inactivation of T-type calcium channels is abolished during the hyperpolarization state, and when the membrane potential recovers to resting levels, the activation of T-type calcium channels depolarizes the membrane potential further to trigger rebound firing. In our SCA42 model mice, this mechanism might be impaired, at least in part, because mutant $Ca_V3.1$ requires greater depolarization to be activated in vitro.

It is generally recognized that T-type calcium channels in ION neurons play crucial roles in amplifying oscillation of the subthreshold membrane potential at their resonant frequency and thereby facilitating the generation of action potential (De Zeeuw et al., 2011; Yarom and Cohen, 2002). In normally matured animals, each PC receives innervation from a single climbing fiber whose soma is located in ION. Owing to the simple one-to-one relationship in the ION-CF-PC pathway, any change in the firing pattern of projection neurons in ION would directly affect PC activity (De Zeeuw et al., 2011). Although we uncovered that the basic property of synaptic transmission onto PCs was not significantly impaired in young KI mice (Fig. 7), the altered ION property revealed in the present study (Fig. 8) may underlie the pathogenesis of SCA, given the proposed importance of oscillatory activity of the olivo-cerebellar circuit in timing control and the generation of complex temporal patterns.

In conclusion, our study demonstrated that the *Cacna1g* p.Arg1723His mutation, corresponding to human *CACNA1G* p.Arg1715His, causes motor dysfunction due to electrophysiological abnormality not only in PCs but also in ION neurons prior to the degeneration of PCs. Among these abnormalities, reduced rebound firing of PCs, which was found in both hereto- and homozygous mutants, is likely to be a cellular basis of the dominantly inherited ataxic phenotype. However, because these abnormalities are unlikely to be direct causes of cellular death, direct pathophysiological mechanisms leading to PC degeneration have yet to be identified. Nevertheless, because our mouse model recapitulates the phenotype (adult onset, gait instability) and pathology (PC degeneration without ubiquitin accumulation) of SCA42 patients, it is appropriate for future evaluation of the efficacy of treatments such as the use of medicinal substances including T-type calcium channel modulators (Jayabal et al., 2016; Shuvaev et al., 2017).

Supplementary data to this article can be found online at https://doi.org/10.1016/j.nbd.2019.104516.

Author contributions

H.D., H.T., K.I., N.Ma., T.I., F.T., contributed to the conception and design of the study; S.H., H.D., M.K., Y.N., M.S., E.S., S.Ko., M.O., H.K., M.S., K.Og., F.H., Y.I., S.Ku., N.H., H.N., K.Tak., A.K., M.T., K.Tan., S.M., N.Mi., H.S., N.S., K.Oz., J.M., H.I., J.Y., S.M., S.T., K.I., N.Ma., T.I., F.T., contributed to the acquisition and analysis of data; S.H., H.D., Y.N., T.Sa., T.Y., H.M., S.T., N.Ma., T.I., F.T., contributed to drafting the text and preparing the figures.

Competing interests

The authors declare no competing financial interests.

Acknowledgments

This work was supported by Grants-in-Aid for Scientific Research (H.D.: 15 K09344, 18 K07503; Y.N.: 17 K07064; T.I.: 18 K06529; S.M.: JP17K10080; N. Miyake: JP16H05357, and N. Matsumoto: P17H01539) from the Japan Society for the Promotion of Science; Grants-in-Aid for Young Scientists (M.K.: 17 K16128; E.S.: 26780411) from the Japan Society for the Promotion of Science; AMED under grant numbers JP18ek0109280, JP18dm0107090, JP18ek0109301, JP18ek0109348, and JP18kk020500; a Health and Labor Sciences Research Grant from the Ministry of Health, Labor and Welfare, Japan (F.T.: #201711060A); Funding from the Collaborative Research Project (2017-#2914) of the Brain Research Institute, Niigata University; the Takeda Science Foundation (H.D., N. Miyake, and N. Matsumoto); the Wakaba Research Fund (Research Fund for Potential Young Researchers) of Yokohama Foundation for Advanced Medical Science (M.K.); Jikei University Research Fund (T.I.); and a Grant for Strategic Research Promotion from Yokohama City University (F.T.: # SK2804).

The authors are grateful to Prof. Toshihiko Momiyama for his support throughout the project. The authors also thank Edanz Group (www.edanzediting.com/ac) for editing a draft of this manuscript.

References

Alfieri, J.A., et al., 2014. Reversible behavioral phenotypes in a conditional mouse model of TDP-43 proteinopathies. J. Neurosci. 34, 15244–15259.

Bavassano, C., et al., 2017. Bicistronic *CACNA1A* gene expression in neurons derived from spinocerebellar Ataxia type 6 patient-induced pluripotent stem cells. Stem Cells Dev. 26, 1612–1625.

Beach, T.G., et al., 2004. Substantia nigra Marinesco bodies are associated with decreased striatal expression of dopaminergic markers. J. Neuropathol. Exp. Neurol. 63, 329–337.

Cain, S.M., Snutch, T.P., 2011. Voltage-gated calcium channels and disease. Biofactors 37, 197–205.

Chemin, J., et al., 2018. De novo mutation screening in childhood-onset cerebellar atrophy identifies gain-of-function mutations in the *CACNA1G* calcium channel gene. Brain 141, 1998–2013.

Coutelier, M., et al., 2015. A recurrent mutation in *CACNA1G* alters Cav3.1 T-type Calcium-Channel conduction and causes autosomal-dominant cerebellar Ataxia. Am. J. Hum. Genet. 97, 726–737.

De Schutter, E., Bower, J.M., 1994. An active membrane model of the cerebellar Purkinje cell. I. Simulation of current clamps in slice. J. Neurophysiol. 71, 375–400.

De Zeeuw, C.I., et al., 2011. Spatiotemporal firing patterns in the cerebellum. Nat. Rev. Neurosci. 12, 327–344.

Engbers, J.D., et al., 2013. Signal processing by T-type calcium channel interactions in the cerebellum. Front. Cell. Neurosci. 7, 230.

Ernst, W.L., et al., 2009. Genetic enhancement of thalamocortical network activity by elevating alpha 1g-mediated low-voltage-activated calcium current induces pure absence epilepsy. J. Neurosci. 29, 1615–1625.

Ferdinandusse, S., et al., 2008. Ataxia with loss of Purkinje cells in a mouse model for Refsum disease. Proc. Natl. Acad. Sci. U. S. A. 105, 17712–17717.

Fujisawa, H., et al., 2016. Chronic hyponatremia causes neurologic and psychologic impairments. J. Am. Soc. Nephrol. 27, 766–780.

Hansen, S.T., et al., 2013. Changes in Purkinje cell firing and gene expression precede behavioral pathology in a mouse model of SCA2. Hum. Mol. Genet. 22, 271–283.

Hsu, P.D., et al., 2013. DNA targeting specificity of RNA-guided Cas9 nucleases. Nat. Biotechnol. 31, 827–832.

Hutcheon, B., Yarom, Y., 2000. Resonance, oscillation and the intrinsic frequency preferences of neurons. Trends Neurosci. 23, 216–222.

Isope, P., Murphy, T.H., 2005. Low threshold calcium currents in rat cerebellar Purkinje cell dendritic spines are mediated by T-type calcium channels. J. Physiol. 562, 257–269.

Jayabal, S., et al., 2015. Rapid onset of motor deficits in a mouse model of Spinocerebellar Ataxia type 6 precedes late cerebellar degeneration. eNeuro 2.

Jayabal, S., et al., 2016. 4-aminopyridine reverses ataxia and cerebellar firing deficiency in a mouse model of spinocerebellar ataxia type 6. Sci. Rep. 6, 29489.

Kelley, L.A., Sternberg, M.J., 2009. Protein structure prediction on the web: a case study using the Phyre server. Nat. Protoc. 4, 363–371.

Kim, D., et al., 2001. Lack of the burst firing of thalamocortical relay neurons and resistance to absence seizures in mice lacking α_{1G} T-type Ca^{2+} channels. Neuron 31, 35–45.

Kimura, M., et al., 2017. SCA42 mutation analysis in a case series of Japanese patients with spinocerebellar ataxia. J. Hum. Genet. 62, 857–859.

Lee, J., et al., 2004. Lack of delta waves and sleep disturbances during non-rapid eye movement sleep in mice lacking $\alpha 1_G$-subunit of T-type calcium channels. Proc. Natl. Acad. Sci. U. S. A. 101, 18195–18199.

Llano, I., et al., 1994. Calcium-induced calcium release in cerebellar Purkinje cells. Neuron 12, 663–673.

Matsumoto-Makidono, Y., et al., 2016. Ionic basis for membrane potential resonance in neurons of the inferior olive. Cell Rep. 16, 994–1004.

Matsushita, K., et al., 2002. Bidirectional alterations in cerebellar synaptic transmission of tottering and rolling Ca^{2+} channel mutant mice. J. Neurosci. 22, 4388–4398.

Molineux, M.L., et al., 2006. Specific T-type calcium channel isoforms are associated with distinct burst phenotypes in deep cerebellar nuclear neurons. Proc. Natl. Acad. Sci. U. S. A. 103, 5555–5560.

Morino, H., et al., 2015. A mutation in the low voltage-gated calcium channel *CACNA1G* alters the physiological properties of the channel, causing spinocerebellar ataxia. Mol. Brain 8, 89.

Ngo, K., et al., 2018. Expanding the global prevalence of spinocerebellar ataxia type 42.

Neurol. Genet. 4, e232.

Orduz, D., Llano, I., 2007. Recurrent axon collaterals underlie facilitating synapses between cerebellar Purkinje cells. Proc. Natl. Acad. Sci. U. S. A. 104, 17831–17836.

Park, Y.G., et al., 2010. $Ca_V3.1$ is a tremor rhythm pacemaker in the inferior olive. Proc. Natl. Acad. Sci. U. S. A. 107, 10731–10736.

Payandeh, J., et al., 2011. The crystal structure of a voltage-gated sodium channel. Nature 475, 353–358.

Perez-Reyes, E., Lory, P., 2006. Molecular biology of T-type calcium channels. CNS Neurol. Disord. Drug Targets 5, 605–609.

Puil, E., et al., 1986. Quantification of membrane properties of trigeminal root ganglion neurons in Guinea pigs. J. Neurophysiol. 55, 995–1016.

Ran, F.A., et al., 2013. Genome engineering using the CRISPR-Cas9 system. Nat. Protoc. 8, 2281–2308.

Rothman, J., Silver, R.A., 2018. NeuroMatic: An integrated open-source software toolkit for acquisition, analysis and simulation of electrophysiological data. Front. Neuroinform. 12, 14.

Sakurai, M., 1990. Calcium is an intracellular mediator of the climbing fiber in induction of cerebellar long-term depression. Proc. Natl. Acad. Sci. U. S. A. 87, 3383–3385.

Sato, K., et al., 2010. Mapping of autosomal dominant cerebellar ataxia without the pathogenic PPP2R2B mutation to the locus for spinocerebellar ataxia 12. Arch. Neurol. 67, 1257–1262.

Schneider, C.A., et al., 2012. NIH image to ImageJ: 25 years of image analysis. Nat. Methods 9, 671–675.

Shakkottai, V.G., et al., 2011. Early changes in cerebellar physiology accompany motor dysfunction in the polyglutamine disease spinocerebellar ataxia type 3. J. Neurosci. 31, 13002–13014.

Shuvaev, A.N., et al., 2017. Progressive impairment of cerebellar mGluR signalling and its therapeutic potential for cerebellar ataxia in spinocerebellar ataxia type 1 model mice. J. Physiol. 595, 141–164.

Simms, B.A., Zamponi, G.W., 2014. Neuronal voltage-gated calcium channels: structure, function, and dysfunction. Neuron 82, 24–45.

Singh, B., et al., 2007. Mutational analysis of *CACNA1G* in idiopathic generalized epilepsy Mutation in brief #962. Online Hum. Mutat. 28, 524–525.

Strom, S.P., et al., 2010. High-density SNP association study of the 17q21 chromosomal region linked to autism identifies *CACNA1G* as a novel candidate gene. Mol. Psychiatry 15, 996–1005.

Tadayonnejad, R., et al., 2010. Rebound discharge in deep cerebellar nuclear neurons in vitro. Cerebellum 9, 352–374.

Talley, E.M., et al., 1999. Differential distribution of three members of a gene family encoding low voltage-activated (T-type) calcium channels. J. Neurosci. 19, 1895–1911.

van Welie, I., et al., 2006. Different levels of Ih determine distinct temporal integration in bursting and regular-spiking neurons in rat subiculum. J. Physiol. 576, 203–214.

Watase, K., et al., 2008. Spinocerebellar ataxia type 6 knockin mice develop a progressive neuronal dysfunction with age-dependent accumulation of mutant $Ca_V2.1$ channels. Proc. Natl. Acad. Sci. U. S. A. 105, 11987–11992.

Wulff, P., et al., 2009. Synaptic inhibition of Purkinje cells mediates consolidation of vestibulo-cerebellar motor learning. Nat. Neurosci. 12, 1042–1049.

Yarom, Y., Cohen, D., 2002. The olivocerebellar system as a generator of temporal patterns. Ann. N. Y. Acad. Sci. 978, 122–134.

Zamponi, G.W., et al., 2015. The physiology, pathology, and pharmacology of voltage-gated calcium channels and their future therapeutic potential. Pharmacol. Rev. 67, 821–870.